

DLR-IB-RM-OP-2017-164

**System Identification and
Parameter Space Control Design for
a Small Unmanned Aircraft**

Bachelor's Thesis

Andre Fialho Coelho



DLR

**Deutsches Zentrum
für Luft- und Raumfahrt**

BACHELORARBEIT

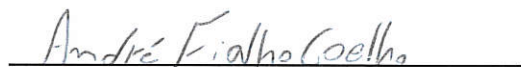
SYSTEM IDENTIFICATION AND PARAMETER SPACE CONTROL DESIGN FOR A SMALL UNMANNED AIRCRAFT

Freigabe:

Der Bearbeiter:

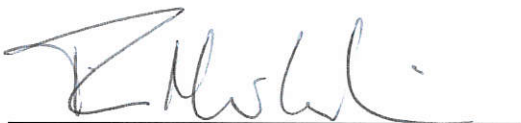
Unterschriften

Andre Fialho Coelho



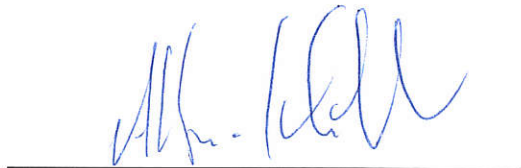
Betreuer:

Tin Muskardin



Der Institutsdirektor

Dr. Alin Albu-Schäffer



Dieser Bericht enthält 57 Seiten, 21 Abbildungen und 22 Tabellen

André Fialho Coelho

System Identification and Parameter Space Control Design for a Small Unmanned Aircraft

Campos dos Goytacazes – Brazil

2017

André Fialho Coelho

System Identification and Parameter Space Control Design for a Small Unmanned Aircraft

Thesis presented to the Instituto Federal Fluminense, Brazil as a partial requisite to the awarding of the five-year Bachelor degree in Control and Automation Engineering.

Instituto Federal de Educação, Ciência e Tecnologia Fluminense - IFF Campos – Centro
Control and Automation Engineering Program

Supervisor: Dr. Alexandre Carvalho Leite
Co-supervisor: Tin Muskardin (German Aerospace Center – DLR)

Campos dos Goytacazes – Brazil

2017

Acknowledgements

I am grateful to God for having helped me in all moments. Without Him nothing would have been possible.

I thank the Instituto Federal Fluminense for having provided me with the means to become a control and automation engineer.

I would also like to express my gratitude to my supervisors, Prof. Alexandre Leite, for teaching me a little about his way of thinking and solving problems, which I have always admired. And Tin Muskardin, for always being solicitous and willing to teach and help, characteristics that make him an admirable engineer and researcher.

I am especially grateful to my family for all love and support. For providing me with a home where I could grow personally and professionally.

A very special gratitude goes to my future wife, Raquel, for always being there for me and unconditionally supporting me in my dream of becoming a good engineer.

Abstract

Initial tests in cooperative control for autonomous landings of an Unmanned Aerial Vehicle (UAV) on a moving car have presented promising results. However, the identification of a high-fidelity simulation model is a step of great importance towards the development of more effective model predictive control strategies, which rely on precise models to allow cooperative control of High Altitude, Long Endurance (HALE) UAVs with autonomous ground vehicles. In this context, this work aims to develop a reliable model for the Penguin BE aircraft used in cooperative landing tests at the German Aerospace Center (DLR), and to design a high-performance pitch attitude controller applying the parameter space approach. The system identification procedure has been carried out by applying both, the Output Error and the Two Step methods, and a linear longitudinal model of the aircraft has been developed. Parameter Space Control has been applied to the identified model in order to suggest a set of alternative gains to the ones that are currently in use, which have been fine-tuned in flight, using the Ziegler-Nichols method, which will not be viable in the scope of stratospheric missions.

Keywords: System identification. Parameter space control design. Output Error Method. Two Step Method. UAV.

List of Figures

Figure 1 – Successful cooperative landing with demonstrator setup.	10
Figure 2 – Elektra One Solar.	10
Figure 3 – Penguin BE UAV.	11
Figure 4 – Simulink® model of Penguin BE, created using AeroSim Blockset. . . .	13
Figure 5 – Example of DLR 3211 input.	15
Figure 6 – Block schematic of the Output Error method.	17
Figure 7 – Details of the OEM-Software.	18
Figure 8 – Simplified aircraft block diagram.	22
Figure 9 – Optimal inputs in the time and frequency domains.	28
Figure 10 – Actual flight data inputs in the time and frequency domains.	29
Figure 11 – Bode plots of derivative terms. The blue, red, and black dashed rectangles represent the regions of identifiability of the phugoid, short period, and throttle doublet maneuvers, respectively.	32
Figure 12 – Inputs used in identification.	34
Figure 13 – Inputs used in validation.	35
Figure 14 – States simulated with the <i>a priori</i> model and measured states.	36
Figure 15 – States simulated with the model resulting from the Output Error Method and measured states.	38
Figure 16 – Measured longitudinal and lateral states and states generated from the integration of the 6DOF equations of motion with estimated biases added.	40
Figure 17 – Reconstructed forces and moments, and forces and moments from linear-regression – validation set.	42
Figure 18 – Measured and Two Step Method simulated states.	43
Figure 19 – Measured States and states resulting from the Output Error and Two Step identified models.	45
Figure 20 – System performance in the parameter space. All specification regions on the left. Intersection of specifications on the right. Left-hand-side plots: yellow – stable system; blue – overshoot less than 5%; green – settling time less than 10 seconds; red – rise time less than 1 second; black – gains currently in use. Right-hand-side plots: black – gains where all specifications are met at the same time; green – gains currently in use.	49
Figure 21 – Intersection of specifications in the three-dimensional parameter space. Black spheres – gains where all specifications are met at the same time; green sphere – gains currently in use	50

List of Tables

Table 1 – Characteristics of the model validation statistic measures	24
Table 2 – Values tuned in flight and grid search range of gains	26
Table 3 – Characteristics of the the optimal elevator and throttle inputs.	27
Table 4 – Characteristics of the inputs from flight data	29
Table 5 – Identifiability of derivatives	33
Table 6 – Statistical measures of the states simulated using the <i>a priori</i> model – identification set	35
Table 7 – Statistical measures of the states simulated using the <i>a priori</i> model – validation set	36
Table 8 – Statistical measures of the states resulting from the Output Error Method – identification set	37
Table 9 – Statistical measures of the states resulting from the Output Error Method – validation set	37
Table 10 – Estimated measurement biases for each maneuver	39
Table 11 – Statistical measures of the reconstructed states – validation set	40
Table 12 – Linear regression terms and respective values	41
Table 13 – Statistical measures of the Two Step Method estimated forces and mo- ments – identification set	41
Table 14 – Statistical measures of the Two Step Method estimated forces and mo- ments – validation set	41
Table 15 – Statistical measures of the Two Step Method forces and moments ob- tained by Lee (2017) – identification set	41
Table 16 – Statistical measures of the Two Step Method forces and moments ob- tained by Lee (2017) – validation set	42
Table 17 – Statistical measures of the states resulting from the Two Step Method – identification set	43
Table 18 – Statistical measures of the states resulting from the Two Step Method – validation set	44
Table 19 – Statistical measures of the Two Step Method states obtained by Lee (2017) – identification set	44
Table 20 – Statistical measures of the Two Step Method states obtained by Lee (2017) – validation set	44
Table 21 – Performance indicators of the actual control system	47
Table 22 – Definition of the concise derivatives	57

List of symbols

u, v, w	Linear velocities along the x, y, and z axes, respectively, in the body frame
a_x, a_y, a_z	Linear accelerations along the x, y, and z axes, respectively, in the body frame
ϕ, θ, ψ	Roll, pitch and yaw angles, respectively
p, q, r	Roll, pitch and yaw rates, respectively
ω	Engine angular velocity
h	Aircraft altitude
X, Z	Axial and normal forces, respectively
M	Pitching moment

Contents

1	INTRODUCTION	8
1.1	Previous work on the application	9
1.2	Penguin BE UAV	9
2	IDENTIFICATION AND CONTROL DESIGN FOR PENGUIN BE .	12
2.1	<i>A priori</i> model	12
2.2	Optimal Input Design	13
2.3	Output Error Method	16
2.3.1	Maximum likelihood estimation and cost function formulation	18
2.4	Two Step Method	19
2.4.1	Flight path reconstruction	20
2.4.2	Estimation of the force and moment components	21
2.5	Model validation	23
2.6	Parameter space control design	24
3	RESULTS AND DISCUSSION	27
3.1	Considerations about the experiment	27
3.2	System identification results	35
3.2.1	Results of the <i>a priori</i> model	35
3.2.2	Results of the Output Error Method	36
3.2.3	Results of the Two Step Method	39
3.2.3.1	Flight path reconstruction results	39
3.2.3.2	Results of force and moment components identification	40
3.2.4	Comparison between identification methods	45
3.3	Results of Parameter Space Control Design	47
4	CONCLUSION AND OUTLOOK	51
	BIBLIOGRAPHY	52
	APPENDIX	56
	APPENDIX A – CONCISE LONGITUDINAL AERODYNAMIC DERIVATIVES AND ENGINE DYNAMICS	57

1 INTRODUCTION

Recent studies being performed at the German Aerospace Center (DLR) aim to develop new technologies in order to land High Altitude, Long Endurance (HALE) Unmanned Aerial Vehicles (UAVs) on a platform mounted on the top of a ground vehicle, which, cooperatively with the UAV, controls position and velocity until successful landing is achieved. The main purpose is to eliminate the need for an aircraft-mounted landing gear and also to facilitate landings in crosswind situations. As a result, the total mass of the aircraft would be significantly reduced. This would allow its operation for long periods of time since this kind of UAVs demands very lightweight structures and at the same time heavy batteries, required for overnight flight. If a reliable integrated landing system for such UAVs is successfully developed, a large step will be taken towards their commercial use. The main advantage of such ultralight stratospheric aircraft consists in its versatility to be applied in numerous applications, including tasks that are usually performed by satellites, e.g. earth observation, atmospheric research, and communication networks. HALE UAVs are attractive options to supplement or substitute satellites due to high costs, necessity of rocket launch, and dependence of orbits intricate to the use of these spacecraft.

Cooperative landings have successfully been performed with the use of a demonstrator setup (Fig. 1), comprised of a Penguin BE small unmanned aircraft and a car with a human driver. However, a high fidelity model of the small UAV is required in order to eliminate or reduce the need for in-flight tuning of control parameters and to further improve the performance of the system through optimal control design. Adding to that, a reliable simulation model of the aircraft would accelerate the process of developing more effective cooperative control strategies to finally allow the first tests with actual HALE UAVs and unmanned ground vehicles. The approach that will be applied, namely Model Predictive Control, aims to generate feasible and optimal trajectories, based on *a priori* knowledge of the vehicles. Therefore, deficient models would compromise the application of such technique.

In this context, this work aims to develop a reliable model for the Penguin BE aircraft used in cooperative landing tests, as well as to analyze the pitch attitude control design that is currently in use and suggest alternative designs within the predefined specifications.

Two different approaches are applied in system identification, namely time-domain Output Error Method and Two Step Method. Control design is performed through the application of a parameter space analysis. The thesis is divided into two major parts:

Chapter 2 provides an explanation of the identification methods being utilized and how they have been applied, as well an overview of the model validation tools adopted. It also provides a presentation of Parameter Space Control Design and the way it has been adapted for the intended application. Furthermore, related papers on each subtopic are also cited in this chapter. In sequence, Chapter 3 presents the results of the identification methods and a comparison between them, as well as the results of control design and analysis in the space of parameters.

1.1 Previous work on the application

Several articles and conference papers about the DLR cooperative landing of HALE UAVs have been published. The concept was firstly introduced by Laiacker et al. (2013), which is mainly focused on the presentation of the multi-sensor system used in the landings. The paper gives specific details about vision-based state estimation and sensor data fusion methods employed.

A couple of years later, Muskardin et al. (2016) presented details about the cooperative control algorithm and the results of the first simulations. Subsequent development and the first results of successful landings with the demonstrator setup are presented by Muskardin et al. (2016). Ultimately, Muskardin et al. (2017) also adds new advances within the application and results of additional landing experiments. The main improvements are the inclusion of vision-based state estimation and some alterations in the the high-level mission control structure in order to provide safer and smoother cooperative landings.

Adding to that, three master's theses have been produced within the field. The first, Balmer (2015), was mainly concerned about modeling, simulation, and development and testing of aircraft control strategies, including Total Energy Control System (TECS) (KASTNER; LOOYE, 2013). The second, Persson (2016), performed a linear analysis of the cooperative system, further developed control strategies, and presented results of the first tests. The third, Lee (2017), aimed to identify high fidelity models for both Penguin BE and the optionally piloted UAV Elektra One Solar¹ (Figure 2). The results and methods applied to Penguin BE system identification are compared with the ones achieved in this work.

1.2 Penguin BE UAV

The aircraft being used in the demonstrator setup, whose longitudinal model is identified in this work, is a Penguin BE UAV (Fig. 3), developed by UAV Factory². It is an

¹ <<https://www.elektra-solar.com/>>

² <<http://www.uavfactory.com/>>



Figure 1 – Successful cooperative landing with demonstrator setup.

Source: Muskardin et al. (2017).



Figure 2 – Elektra One Solar.

Source: Lee (2017).

electric high-wing unmanned aerial vehicle with a negative V-tail configuration, powered by a 640 Wh battery cartridge made from 48 lithium-polymer cells. Besides that, this aircraft is propelled by a geared brushless DC motor and a 19×11 inch propeller in pusher configuration. Furthermore, it has 3.3 meters of wing span and 2.27 meters of length. Its empty weight, including battery cartridge and standard landing gear, is 14.9 kg with a maximum payload capacity of 6.6 kg (UAV FACTORY).



Figure 3 – Penguin BE UAV.

Source: UAV Factory.

The DLR's Penguin BE UAV instrumentation provides measurements of the variables used in system identification. A LORD MicroStrain³ 3DM-Gx3-25 inertial measurement unit (IMU) measures linear accelerations, angular velocities and orientation, at a sampling rate of 100 Hz. The Swiss Air-Data⁴ PSS-8 pitot-static system, mounted on the nose of the aircraft, provides true airspeed and temperature data, at a 20 Hz sampling rate. The Novatel⁵ Flex-Pak6 RTK receiver comprises a differential GPS and is responsible for measuring latitude, longitude and altitude, at a sampling rate of 20 Hz. In addition, a wireless local-area network (WLAN) sets up the communication with the ground station.

³ <<http://www.microstrain.com/>>

⁴ <<http://www.swiss-airdata.com/>>

⁵ <<http://www.novatel.com/>>

2 IDENTIFICATION AND CONTROL DESIGN FOR PENGUIN BE

2.1 *A priori* model

The first attempt to model and simulate the DLR's Penguin BE aircraft was performed by Balmer (2015). In his master's thesis, Balmer developed a Simulink® model of the aircraft, which was created using the AeroSim Blockset (UNMANNED DYNAMICS). In order to model the aerodynamics, an integration of the potential flow solver named Athena Vortex Lattice (AVL) (DRELA; YOUNGREN, 2004) and a program for the design and analysis of subsonic isolated airfoils, XFOIL (DRELA; YOUNGREN, 2000), was performed, according to the method described in Klöckner (2013). Furthermore, a propulsion model was developed from both, experimental data and information provided by the manufacturer. In order to estimate the total moment of inertia, the aircraft components were modeled as hollow hulls (fuselage), flat plates (wings and tail), or point masses (other parts). Then the aircraft states have been calculated by introducing the modeled forces and moments into the six-degree-of-freedom (6DOF) nonlinear equations of motion. An overview of the resulting model can be seen in Figure 4.

As mentioned by Balmer (2015), the conceived model presented inaccuracies which compromised its use in inner-loop control design; therefore control parameters had to be re-tuned in flight by applying the Ziegler-Nichols method.

Despite the mentioned inaccuracies, a work developed by Persson (2016) described an effort to obtain a linear model of the Penguin BE UAV through trim and linearization of the Simulink model presented by Balmer (2015). The resulting state-space model describing the longitudinal dynamics of the aircraft is given in Equation 2.1.

$$\begin{bmatrix} \dot{u} \\ \dot{w} \\ \dot{q} \\ \dot{\theta} \\ \dot{\omega} \end{bmatrix} = \begin{bmatrix} -0.10 & 0.39 & -1.4 & -9.8 & 0.006 \\ -0.64 & -3.6 & 22 & -0.6 & 0 \\ 0.19 & -2.8 & -5.6 & 0 & -0.001 \\ 0 & 0 & 1 & 0 & 0 \\ 21 & 1.2 & 0 & 0 & -2.6 \end{bmatrix} \begin{bmatrix} u \\ w \\ q \\ \theta \\ \omega \end{bmatrix} + \begin{bmatrix} 0.38 & 0 \\ -7.3 & 0 \\ -65 & 0 \\ 0 & 0 \\ 0 & 2027 \end{bmatrix} \begin{bmatrix} \delta_e \\ \delta_t \end{bmatrix} \quad (2.1)$$

where u and w are the linear velocities along x and z axes, respectively, in the body frame; q corresponds to the pitch rate; θ denotes the pitch angle; and ω represents the engine angular velocity. δ_e and δ_t are the elevator and throttle commands, respectively. All states and measurements are in the International System of Units (SI).

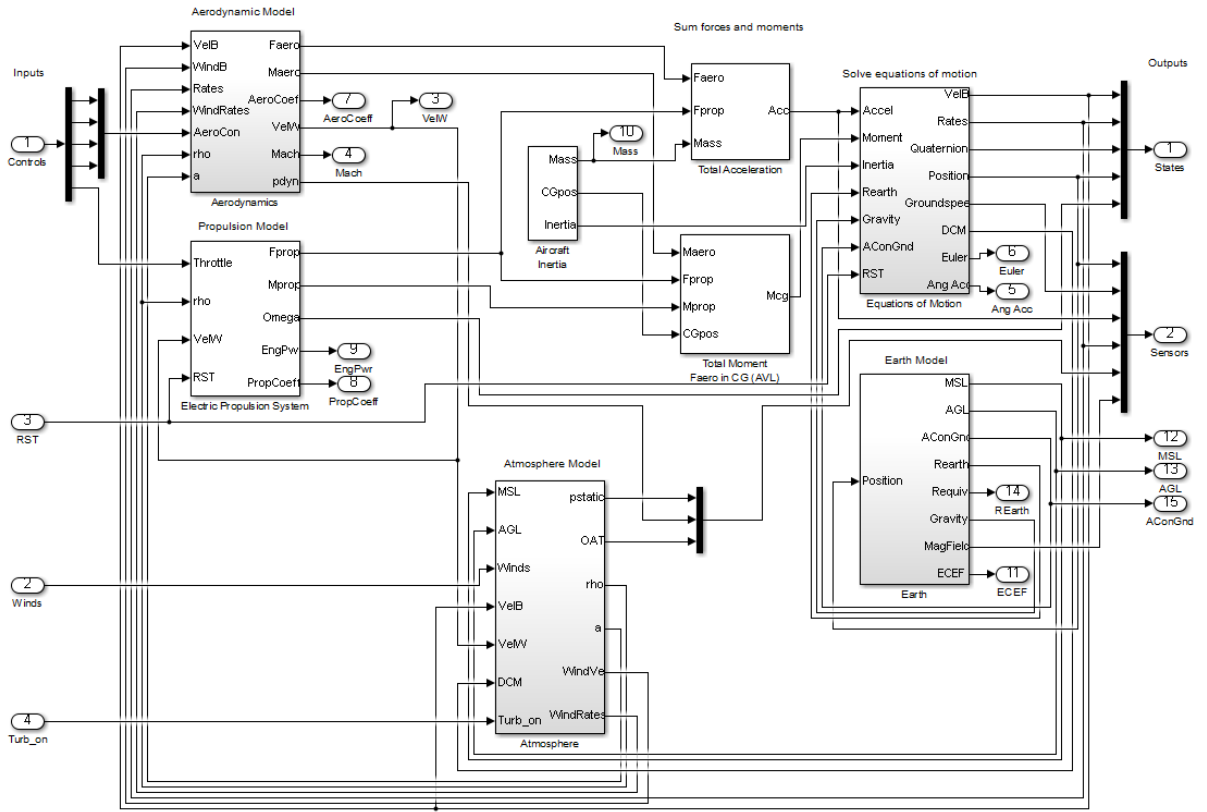


Figure 4 – Simulink® model of Penguin BE, created using AeroSim Blockset.

Source: Balmer (2015).

The system has a total of five poles, with one real pole from engine dynamics and two complex-conjugate pairs related to the phugoid and short period modes, described in Section 2.2.

Phugoid:	$-0.03072 \pm 0.5349j$
Short period:	$-4.5935 \pm 7.7958j$
Engine dynamics:	-2.6515

Being the most accurate linear representation of the aircraft available, this setup has been used in this work as *a priori* model.

2.2 Optimal Input Design

The optimal input design process consists of defining a set of maneuvers, based on *a priori* knowledge of the system, which best excite the aircraft modes, in an attempt to maximize the effect of their dynamics in the measurements of the states. This step is crucial to aircraft system identification since the estimation of a given parameter is impossible unless its variation affects the data being analyzed. Therefore, the accuracy and reliability

of estimates are closely attached to how much information about the desired parameter is available in the measured response. This amount of information, in turn, clearly depends on the nature of the given input for linear and nonlinear dynamical systems, including aircraft (SHANNON, 1948).

Since Milliken Jr. (1947), the design of proper inputs has been widely considered as a step of great importance for aircraft parameter estimation purposes. Much work has been performed in the area up to date. Mehra (1974), Hamel and Jategaonkar (1996) present reviews on the topic. Qian, Nadri and Dufour (2017) is a more recent study on the application, focused on nonlinear system identification.

According to Jategaonkar (2015), two approaches are commonly applied to optimal maneuver design. The first is based on statistical properties of the estimate and is performed by assuming that the amount of information about a specific parameter in the data being analyzed is a function of the overall model and of the inputs given. Therefore, by keeping the parameters fixed at some *a priori* values, the variation of the information content will be mainly determined by the inputs applied to the system. That being performed, an optimization procedure, having input shape as parameter, is carried out with the intent of achieving the maximum amount of information. This is usually determined by the Fisher matrix (FISHER, 1934), given by Equation 2.2.

$$F_{ij} = E \left\{ \frac{\partial^2 \ln p(z | \Theta)}{\partial \Theta_i \partial \Theta_j} \right\} \quad (2.2)$$

where $p(z | \Theta)$ represents the conditional probability density function of measurements z with respect to a parameter vector Θ , and $E\{\cdot\}$ denotes the expected value. A more detailed view on the statistical approach can be found in Gupta and Hall Jr. (1975), where both, time and frequency domain input designs are demonstrated.

The second approach, which is used in this work, is an engineering approach based on the frequency of the aircraft eigenmodes. In this method, the natural frequencies of an *a priori* model of the aircraft are computed, and input signals are conveniently designed to exhibit maximum energy around those frequencies. This approach is based on the principle that deterministic signals can be represented by a linear combination of complex exponentials in the time domain, which represent components with a specific amplitude at a specific point in the frequency domain. This is achieved by computing the Fourier Transform of the signals (FOURIER, 1878). Therefore, a set of multistep inputs are conveniently designed to exhibit larger components in a sufficiently wide range of frequencies to excite the natural vibrations of the *a priori* model. The use of multistep signals is also justified by their relative easiness to be applied manually. Other types of signals like the Mehra input and the DUT input may also be used (PLAETSCHKE; SCHULZ, 1979). However, these approaches lead to continuous smoothly-varying maneuvers and usually require an

autopilot to be properly performed.

For the purpose of this work, only the longitudinal aircraft modes are to be excited, namely phugoid (or long period) and short period. The phugoid is a lightly damped low-frequency oscillation (generally between 0.1 rad/s and 1 rad/s) in the axial velocity u , which is also visible in pitch attitude θ , altitude h , and, to a lesser extent, in angle of attack α and pitch rate q . The short period mode, in contrast, is a damped high-frequency oscillation (typically between 1 rad/s and 10 rad/s) in the pitch attitude θ , which mainly affects pitch rate q and angle of attack α (COOK, 2012).

According to Jategaonkar (2015), since the short period mode is well damped, it requires a fast changing input to excite it. The signal used to induce this oscillation was the so called DLR 3211 (KALETKA et al., 1989), which consists of a pulse with three time steps (Δt) duration and amplitude of 0.8, another pulse with $2\Delta t$ and amplitude of -1.2, followed by one positive and one negative pulse of duration Δt each and amplitude of 1.1. In this case, the amplitudes presented correspond to the ratio between the amplitude of each pulse and the average absolute value of all amplitudes in the maneuver. An example of the DLR 3211 input is shown in Figure 5.

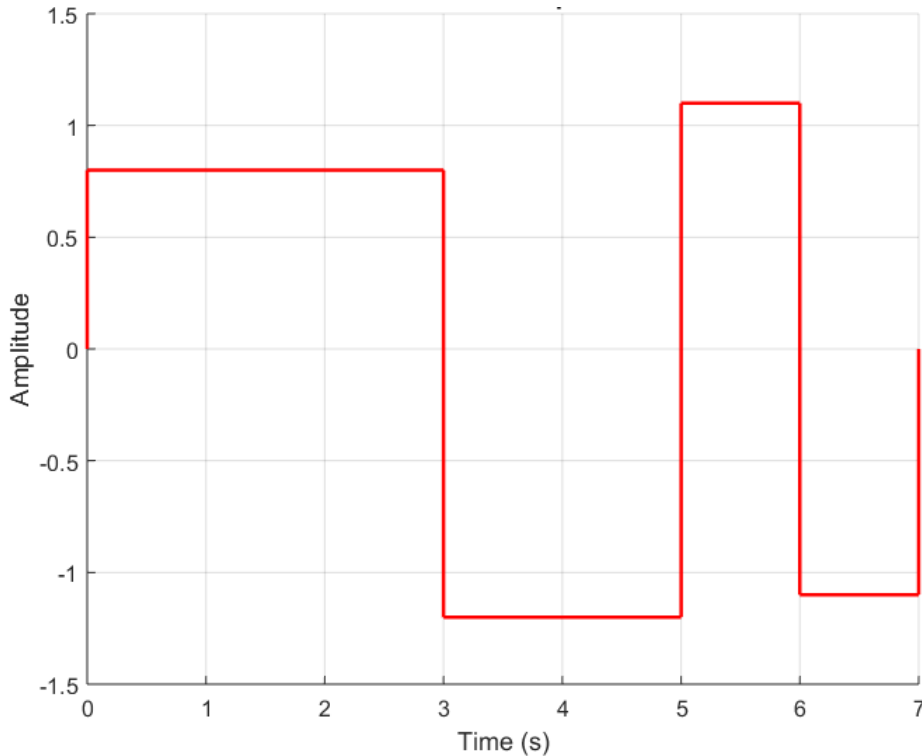


Figure 5 – Example of DLR 3211 input.

Source: The author.

The phugoid mode, being lightly damped, can be satisfactorily excited by a pulse signal. A suitable Δt for the phugoid maneuver has been chosen such that its bandwidth is large enough to account for uncertainties in the *a priori* model and its energy is not

unnecessarily spread over an excessively large range of frequencies. In addition, a throttle doublet has also been used to excite the long period motion in order to identify the effect of the engine dynamics in the system. A doublet in thrust is usually used for this purpose; however a satisfactory model of the aircraft engine has not yet been obtained and the relationship between throttle and thrust has not been mapped yet. The time steps of the doublet and DLR 3211 maneuvers have been calculated such that their energy peak is at the natural frequency of the mode they are intended to excite. The formulas presented in Jategaonkar (2015) to achieve optimal time steps for the doublet and DLR 3211 maneuvers are presented in Equations 2.3 and 2.4, respectively.

$$\Delta t_{DBLT} = \frac{2.3}{\omega_n} \quad (2.3)$$

$$\Delta t_{3211} = \frac{1.6}{\omega_n} \quad (2.4)$$

where Δt_{DBLT} and Δt_{3211} denote the time steps of the doublet and DLR 3211 maneuvers, respectively, and ω_n is the undamped natural frequency of the mode to be excited.

Jategaonkar (2015) also states that, for parameter identification, the system should be allowed to oscillate freely for at least one period of oscillation of the intended motion.

The designed maneuvers have been used as inputs to the Simulink[®] model presented by Balmer (2015). Their amplitudes have been adjusted to avoid instability and actuator saturations.

Ultimately, Bode plots containing the frequency response of each term of the *a priori* model have been used to check if the set of designed maneuvers is sufficient to estimate all derivatives. “Term”, in this case, is used to denote the product of a concise derivative and a state, e.g. $x_u u$. In this stage a rule of thumb, presented by Plaetschke and Schulz (1979) is used. This criterion states that a derivative is not considered identifiable unless its term represents at least 10% of the largest term’s magnitude in the maneuver frequency range.

2.3 Output Error Method

According to Jategaonkar (2015), the Output Error Method (OEM) is the most widely adopted approach in time-domain aircraft parameter estimation from measured flight data (WANG; ILIFF, 2004; MORELLI; KLEIN et al., 2005). It consists of iteratively adjusting model parameters in order to minimize the error between measured data, from flight tests, and predicted data, from integration of state-space model equations.

In the application of this method, the state-space setup presented in Section 2.1 has been adopted as *a priori* model. The derivatives considered identifiable according to

the 10% rule, presented in Section 2.2, have been estimated for a satisfactory fit between the measured and simulated states. In addition, constant terms have been added to the state equations in order to account for measurement biases. On that account, the system has been considered to be as shown in Equation 2.5.

$$\begin{aligned}\dot{x}(t) &= Ax(t) + Bu(t) + b_x, \quad x(t_0) = x_0 \\ y(t) &= Cx(t) + b_y\end{aligned}\tag{2.5}$$

where b_x and b_y correspond to state and measurement bias vectors, respectively.

The Output Error system identification has been carried out through the application of the OEM-Software, presented by Jategaonkar (2015), with some minor modifications. Figures 6 and 7 display the block schematics of the Output Error Method and its implementation within the OEM-Software, respectively.

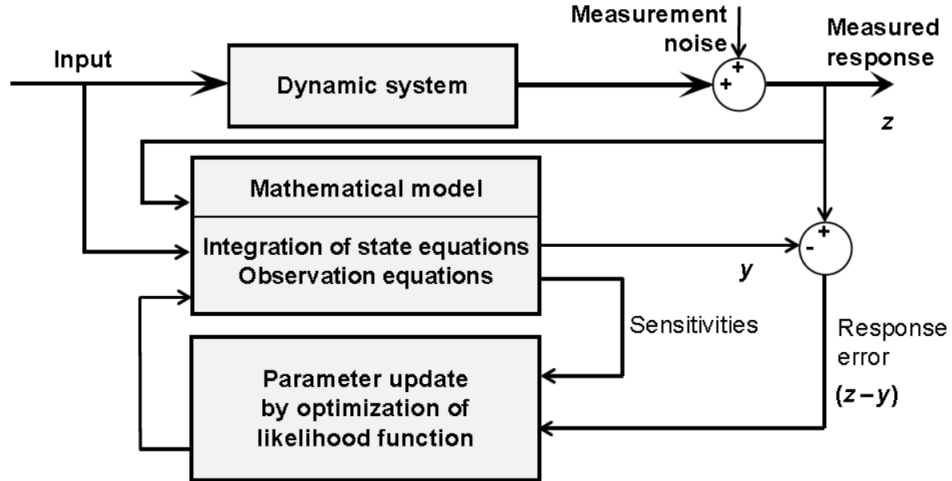


Figure 6 – Block schematic of the Output Error method.

Source: Jategaonkar (2015).

The major steps taken in this work to achieve minimum output error followed the guidelines presented in Jategaonkar (2015), which are

1. Setting initial values of the parameters according to the *a priori* model.
2. Computing the outputs of the model through integration of the state equations, and comparing them with measurements.
3. Estimating the measurement noise covariance matrix.
4. Minimizing the cost function defined in Equation 2.9.
5. Iterating on step two and checking for convergence.

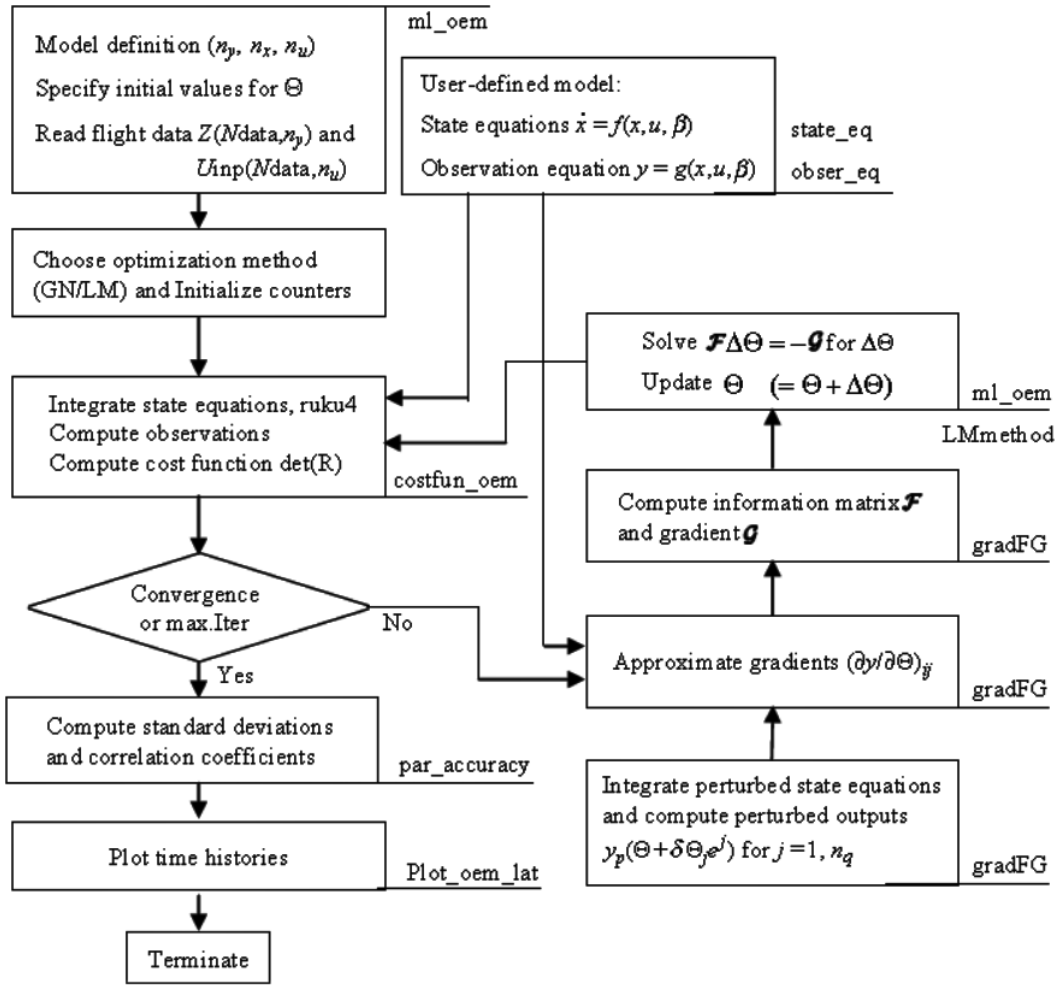


Figure 7 – Details of the OEM-Software.

Source: Jategaonkar (2015).

The minimization of the cost function has been performed through the application of the Levenberg-Marquadt method (JATEGAONKAR, 2015). In addition, the state equations have been numerically integrated by a fourth-order Runge-Kutta integration method, which is included in the OEM-Software (JATEGAONKAR, 2015). Furthermore, the error between the measurements and model outputs has been minimized and optimal parameters have been obtained through maximum likelihood estimation.

2.3.1 Maximum likelihood estimation and cost function formulation

The maximum likelihood estimation is based on the maximization of the likelihood function, defined in Equation 2.6 (FISHER, 1925).

$$p(z \mid \Theta) = \prod_{k=1}^N p(z_k \mid \Theta) \quad (2.6)$$

where $p(z \mid \Theta)$ is the probability of a set of N observations z , given the unknown parameter vector Θ .

The procedure consists of finding suitable values of Θ that maximize $p(z \mid \Theta)$. Contrasting to what is performed in the statistical approach of optimal input design (see Section 2.2), in the Output Error Method, inputs recorded during the flight test are applied and model parameters are varied in order to maximize the likelihood function. For the sake of the fact that $p(z \mid \Theta)$ is usually exponential, its negative logarithm is commonly utilized to find optimal parameters, without affecting the solution. The expression of the logarithm of the probability density function p with respect to measurements z , parameters Θ , and the measurement error covariance matrix, R , is given in Equation 2.7. (JATEGAONKAR, 2015)

$$L(z \mid \Theta, R) = \frac{1}{2} \sum_{k=1}^N \left([z(t_k) - y(t_k)]^T R^{-1} [z(t_k) - y(t_k)] + \frac{N}{2} \ln [\det(R)] + \frac{N n_y}{2} \ln (2\pi) \right) \quad (2.7)$$

where $z(t_k)$ and $y(t_k)$ represent the measurements and model outputs, respectively, and n_y is the number of system outputs.

The error covariance matrix, R , is defined in Equation 2.8.

$$R = \frac{1}{N} \sum_{k=1}^N \left([z(t_k) - y(t_k)][z(t_k) - y(t_k)]^T \right) \quad (2.8)$$

The set of parameters that ensure maximum likelihood between flight measurements and model outputs result from the minimization of Equation 2.7. The cost function can be simplified to Equation 2.9 (JATEGAONKAR, 2015).

$$J(\Theta) = \det(R) \quad (2.9)$$

This definition of the cost function ensures the computational feasibility of the method.

2.4 Two Step Method

The Two Step Method is a system identification procedure comprised of two stages, namely flight path reconstruction (LOMBAERTS et al., 2010; TEIXEIRA et al., 2011; MULDER et al., 1999) and estimation of force and moment parameters through linear regression. Its advantages are the possibility of estimating measurement biases independently from derivative terms, avoiding correlations between these quantities, the

elimination of the need for initial guesses for the parameters, and the assurance of global minimum convergence within two iterations in the second stage. This approach has been performed by numerous authors, including Grymin and Farhood (2016), Grymin (2013), and Oliveira et al. (2005). Lee (2017) has performed two step system identification of the same aircraft analyzed in this work; however a stochastic approach based on an Extended Kalman Filter (EKF) has been applied in first step, rather than the deterministic one, based on maximum likelihood estimation, performed in this composition. Martin and Feik (1982), Evans et al. (1985), and Jategaonkar (2015) state that both procedures usually yield similar results; however the deterministic approach is more advantageous when there is no accurate *a priori* knowledge about noise statistics.

2.4.1 Flight path reconstruction

Flight path reconstruction, also known as data compatibility check, consists in verifying the compatibility of measured data by inputting the variables recorded during flight into the 6DOF rigid-body kinematic equations. This allows for the estimation of instrument errors present in the measurements. The procedure is also performed using the OEM-Software presented in Section 2.3.

In this stage both lateral and longitudinal measurements are used, although only estimates of errors present in the latter are adopted as inputs to the next step.

The nonlinear state equations used in this stage are shown in Equation 2.10.

$$\begin{aligned}
 \dot{u} &= -(q_m - \Delta q)w + (r_m - \Delta r)v - g \sin \theta + (a_{xm}^{CG} - \Delta a_x) , & u(t_0) &= u_0 \\
 \dot{v} &= -(r_m - \Delta r)u + (p_m - \Delta p)w - g \cos \theta \sin \phi + (a_{ym}^{CG} - \Delta a_y) , & v(t_0) &= v_0 \\
 \dot{w} &= -(p_m - \Delta p)v + (q_m - \Delta q)u - g \cos \theta \cos \phi + (a_{zm}^{CG} - \Delta a_z) , & w(t_0) &= w_0 \\
 \dot{\phi} &= (p_m - \Delta p) + (q_m - \Delta q) \sin \phi \tan \theta + (r_m - \Delta r) \cos \phi \tan \theta , & \phi(t_0) &= \phi_0 \\
 \dot{\theta} &= (q_m - \Delta q) \cos \phi - (r_m - \Delta r) \sin \phi , & \theta(t_0) &= \theta_0 \\
 \dot{\psi} &= (q_m - \Delta q) \sin \phi \sec \theta + (r_m - \Delta r) \cos \phi \sec \theta , & \psi(t_0) &= \psi_0 \\
 \dot{h} &= u \sin \theta - v \cos \theta \sin \phi - w \cos \theta \cos \phi , & h(t_0) &= h_0
 \end{aligned} \tag{2.10}$$

where v denotes the aircraft's linear velocity along the y-axis in the body frame; ϕ and ψ represent the roll and yaw angles; h stands for the aircraft altitude; p_m , q_m , and r_m are the measured angular rates; a_{xm}^{CG} , a_{ym}^{CG} , and a_{zm}^{CG} are the measured linear accelerations at the aircraft center of gravity; Δ stands for biases in the measured quantities.

The OEM-Software compares the integrated state equations and calculates the biases through maximum likelihood estimation (see Section 2.3). The procedure is run iteratively in order to minimize errors between the model outputs and measured data. A good match means that the estimated biases are similar to the ones present in the

measurements. This is performed through the minimization of the cost function presented in Equation 2.9, with instrument biases as parameters. In this part, different biases for each maneuver were considered, as suggested by Jategaonkar (2015).

Once the biases are estimated, the longitudinal forces and moments, which were acting on the aircraft during the flight experiment, could be reconstructed from the corrected linear accelerations and angular rates. Since the maneuvers performed were meant to excite only the longitudinal dynamics, the estimates of biases in lateral motion are not reliable.

2.4.2 Estimation of the force and moment components

The second stage of the Two Step Method is a linear regression of the force and moment equation parameters. After an estimate of the linear accelerations and angular rates has been obtained, the total longitudinal forces and moments (aerodynamic and propulsion) have been reconstructed from the corrected measurements. However, in order to obtain mathematical expressions for the forces and moments, it is necessary to discover the contributions of each state and input to the result of the previous step. In order to accomplish that, the expressions for the total longitudinal forces and moments are considered to be a linear combinations of states and inputs, as shown in Equation 2.11.

$$\begin{aligned} X &= X_0 + X_u u + X_w w + X_q q + X_{\delta e} \delta e + X_{\delta t} \delta t \\ Z &= Z_0 + Z_u u + Z_w w + Z_q q + Z_{\delta e} \delta e \\ M &= M_0 + M_u u + M_w w + M_q q + M_{\delta e} \delta e \end{aligned} \tag{2.11}$$

where X , Z , and M correspond to the reconstructed axial and normal forces, and the pitching moment, respectively. The components that multiply inputs and states on the right-hand side are constant terms that define the amount of force or moment that is generated by each variable. These terms correspond to the first-order terms of the Taylor series expansion of the left-hand side variables with respect to each of the right-hand side ones. In addition, subscript 0 means constant biases in the force and moment equations.

The constant terms of the equations are initially set to zero, and their optimal values are obtained through Levenberg-Marquadt minimization of the adapted maximum likelihood cost function (Equation 2.9). This aims to achieve the best fit between the reconstructed forces and moments and the ones generated by the linear polynomials from Equation 2.11. This entire procedure is run through an adaptation of the OEM-Software. The minimization procedure is terminated after two iterations. Since the model is linear in parameters and in the independent variables, convergence is achieved within one iteration; however the software needs a second iteration to check if the minimum value has been encountered.

The Two Step Method results in linear expressions for the total forces and moments acting on the aircraft. However, if a linear state-space model of the overall aircraft is required, the 6DOF equations of motion have to be linearized as well. Figure 8 shows a simplified block diagram of a nonlinear aircraft simulation model. In the Two Step Method, a linear model for the dashed rectangle (total forces and moments) has been obtained; however the 6DOF equations of motion have been used in their nonlinear form during the identification procedure.

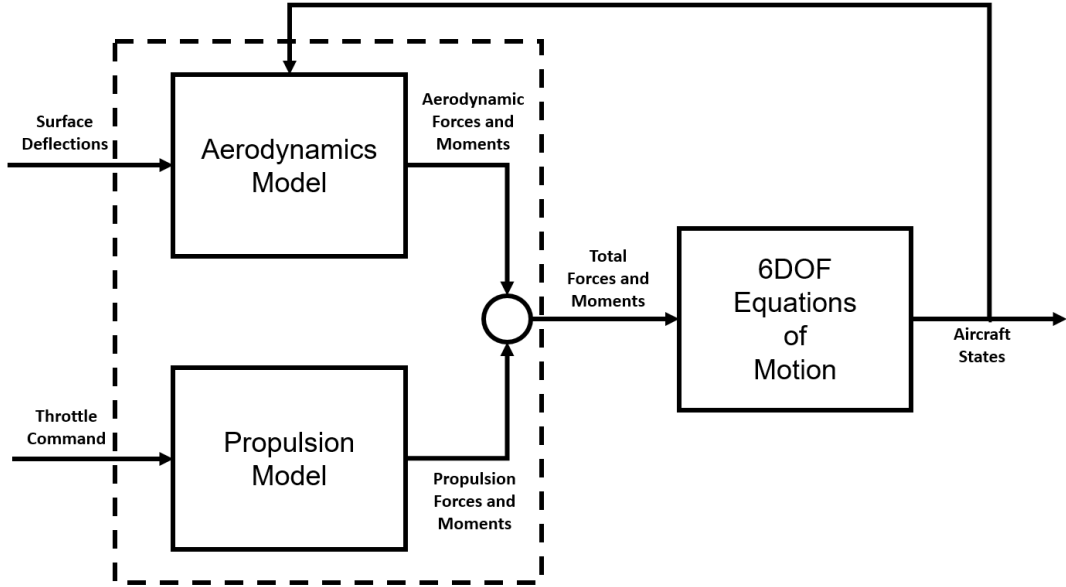


Figure 8 – Simplified aircraft block diagram.

Source: The author.

In order to analyze the match between the measured states and the ones resulting from the Two Step Method, the longitudinal states have been generated by inputting the estimated forces and moments into the longitudinal 6DOF dynamic equations. The measurements of the lateral states are included, as well as the lateral angular rates measurements corrected with the estimated biases, as shown in Equation 2.12.

$$\begin{aligned}
 \dot{u} &= \frac{X}{m} - qw + (r_m - \Delta r)v_m - g \sin \theta \\
 \dot{w} &= \frac{Z}{m} - (p_m - \Delta p)v_m + qu - g \cos \theta \cos \phi_m \\
 \dot{q} &= \frac{1}{I_{yy}} \left(M + ((r_m - \Delta r)^2 - (p_m - \Delta p)^2)I_{xz} + (p_m - \Delta p)(r_m - \Delta r)(I_{zz} - I_{xx}) \right) \\
 \dot{\theta} &= q \cos \phi_m - (r_m - \Delta r) \sin \phi_m
 \end{aligned} \tag{2.12}$$

where m is the aircraft mass; I_{yy} , I_{zz} , I_{xx} , and I_{xz} denote the aircraft moments of inertia and a product of inertia with respect to the axes indicated in the subscripts; X , Z , and

M are the estimated longitudinal forces and moments; subscript m stands for measured lateral variables, and Δ denotes the estimated biases in lateral angular rates.

2.5 Model validation

Model validation, as defined by Schlesinger et al. (1974), is an essential process to judge the applicability of the identified models to the intended purpose. It is performed by checking whether the simulated and measured data match.

In order to provide means of comparing results with Lee (2017), the model validation performed in this work has followed the same procedure presented by Lee.

The simulated states, obtained from both identification methods, have been evaluated by two statistical measures, namely Goodness of Fit (GOF) and Theil's Inequality Coefficient (TIC). The former is a residual analysis criterion to measure model fit, which can be evaluated by multiple statistical metrics. In this project, the normalized mean square error (NMSE) is used as GOF metric. Its definition is given in Equation 2.13.

Theil's Inequality coefficient (Eq. 2.14), according to Jategaonkar (2015), provides more insight about the correlation between measured and simulated data than the GOF. In the process of comparing estimates of dynamic system states, the NMSE measure can be inadequate. As far as this metric concerned, even a straight line may be considered better than a signal that is out of phase with the reference. According to Jategaonkar (2015), values of $TIC < 0.3$ indicate good agreement.

NMSE varies between $-\infty$ and 1, where negative values mean that a straight line matches the reference better than the estimated value, with $-\infty$ as the worst possible fit. Positive values indicate that the estimate fits better than a straight line. A value of one means perfect match between the data. TIC values range between 0 and 1, and the lower its values, the better the fit.

On the other hand, three statistical analyses have been applied in order to follow what has been performed by Lee (2017) in the evaluation of the estimated forces and moments. R^2 , root mean square error (RMSE), and normalized root mean squared error (NRMSE) are defined by Equations 2.15, 2.16, and 2.17, respectively. R^2 varies between 0 and 1. Zero indicates that the estimate fits worse than a straight line, and one means a perfect match.

RMSE is also known as the fit standard error. It has the same unit as the dependent variable. Smaller values of this measure indicate better fit. NRMSE, on the other hand, is the value RMSE divided by the variable range, which makes this measure dimensionless.

$$GOF_i = NMSE_i = 1 - \frac{\|z_i(t_k) - y_i(t_k)\|^2}{\|z_i(t_k) - \bar{z}_i(t_k)\|^2}, \quad i = 1, 2, \dots, n_y \quad (2.13)$$

$$TIC_i = \frac{\sqrt{\frac{1}{N} \sum_{k=1}^N [z_i(t_k) - y_i(t_k)]^2}}{\sqrt{\frac{1}{N} \sum_{k=1}^N [z_i(t_k)]^2} + \sqrt{\frac{1}{N} \sum_{k=1}^N [y_i(t_k)]^2}}, \quad i = 1, 2, \dots, n_y \quad (2.14)$$

$$R_i^2 = 1 - \frac{\sum_{i=1}^N [z_i(t_k) - y_i(t_k)]^2}{\sum_{i=1}^N [z_i(t_k) - \bar{z}_i(t_k)]^2}, \quad i = 1, 2, \dots, n_y \quad (2.15)$$

$$RMSE_i = \sqrt{\frac{\sum_{i=1}^N [z_i(t_k) - y_i(t_k)]^2}{N}}, \quad i = 1, 2, \dots, n_y \quad (2.16)$$

$$NRMSE_i = \frac{RMSE_i}{z_{max} - z_{min}}, \quad i = 1, 2, \dots, n_y \quad (2.17)$$

In Equations 2.13 through 2.17, N is the total number of data points, and n_y is the total number of system outputs. z and y are the measurement and model output vectors, respectively. \bar{z} is the mean value of z , and $\|\cdot\|$ indicates the 2-norm of a vector.

A summary of the characteristics of the statistical measures used in this work is presented in Table 1. The column named “Variables” stands for the variables evaluated by each measure, according to what has been performed by Lee (2017). All measures can be interchangeably used to evaluate states, forces, and moments. However, in order to allow a comparison with the results obtained by Lee (2017), the measures have been applied in the same way. The column named “Threshold” defines the limits that indicate good agreement between measurements and estimates. Except for TIC, a threshold for the other measures could not be found in the aircraft system identification literature.

Table 1 – Characteristics of the model validation statistic measures.

Measure	Range	Worst match	Best match	Threshold	Variables (LEE, 2017)
GOF (NMSE)	$-\infty \sim 1$	$-\infty$	1	undefined	states
TIC	$0 \sim 1$	1	0	<0.3	states
R^2	$-\infty \sim 1$	$-\infty$	1	undefined	forces and moments
RMSE	$0 \sim +\infty$	$+\infty$	0	undefined	forces and moments
NRMSE	$0 \sim 1$	1	0	undefined	forces and moments

Source: The author.

2.6 Parameter space control design

Parameter space control design is a widely used approach in robust control applications. It consists of designing a control system to meet some stability and/or performance specifications by conducting a study on how the controlled plant will behave with respect to parameter variations (ACKERMANN, 1980). In robust control applications, both control and plant parameters are taken into account, which usually includes controller and model

variations, quantization effects, and sensor failures. The objective is to find a controller that behaves satisfactorily even if anomalous system variations occur. An application of this approach is described by Ackermann (2008), where the author cites his effort to find a set of fixed gains for an aircraft control system, instead of performing gain scheduling.

Ackermann (2012) and Lavretsky and Wise (2013) are books on robust control, which give a detailed explanation of the parameter space approach. Demirel and Guvenc (2010) and Saeki (2013) present cases where the technique has been applied.

The aim of this work slightly differs from robust control design objectives; however, a similar procedure is applied. The goal is to analyze the PID control parameter space for a set of predefined stability and performance requirements and check whether the currently used control gains fall inside or close to the intersection of the specifications when applied to the identified model. These gains have been tuned in flight using the Ziegler-Nichols method, which does not require a model. Similar performance of the in-flight-tuned controller would be a possible indicator that the model is suitable for control design. This would eliminate the necessity of in-flight re-tuning and also allow for optimal control design.

In order to perform that analysis, a grid search has been performed in a region around the currently used gains. Multiple combinations of proportional, integral, and derivative gains have been tested to check if the resulting closed-loop system would meet the specifications.

For the purpose of this work, only the pitch attitude control system has been analyzed, whose control law is given in Equation 2.18.

$$\delta_e = -\left(K_\theta + \frac{K_{i\theta}}{s}\right)(\theta_{des} - \theta) - K_q(q_{turn} - q) \quad (2.18)$$

where K_θ , $K_{i\theta}$, and K_q are the proportional, integral and derivative gains, respectively. θ and q are the measured aircraft pitch angle and angular rates. θ_{des} is the reference for θ and q_{turn} is the reference for q , which is used for coordinated turns.

The requirements are: stable system, overshoot less than 5%, rise time (T_r) less than 1 second, and settling time (T_s), 5% criterion, less than 10 seconds. The result of the analysis is a set of plots. Each specification corresponds to a circle of a specific color. Circles are plotted in the coordinates corresponding to the parameters being tested, in case the closed-loop system meets that requirement. A total of four plots have been generated, namely $K_\theta \times K_{i\theta}$, $K_\theta \times K_q$, $K_q \times K_{i\theta}$ (Fig. 20), and a three-dimensional figure (Fig. 21). The gains that are currently being adopted and the range where the grid search has been run are shown in Table 2.

The ranges of gains have been chosen such that the behavior of the system could be analyzed in multiple points around the gains tuned in flight. The range of K_θ has been

Table 2 – Values tuned in flight and grid search range of gains.

Gain	Currently adopted value	Grid search range
K_θ	1	0.9 \sim 1.2
$K_{i\theta}$	0.14 s^{-1}	0.05 \sim 0.4 s^{-1}
K_q	0.2 s	0.1 \sim 0.4 s

Source: The author.

defined not to cover gains much greater than 1. This value caused small occasional actuator saturations during the flight, which did not compromise the efficacy of the control system. The gains $K_{i\theta}$ and K_q have been initially set to range between 0.1 and 0.4 seconds $^{-1}$, for the former, and 0.1 and 0.4 seconds, for the latter. However, in order to find a minimum value of $K_{i\theta}$ that would not comply with the specifications for any values of the other two gains, the lower bound of its range has been slightly decreased to 0.05 seconds $^{-1}$. The step of variation for all gains has been set to 0.01.

3 RESULTS AND DISCUSSION

3.1 Considerations about the experiment

The natural frequencies of the *a priori* model are: 0.5358 rad/s and 9.0485 rad/s (0.085 Hz and 1.44 Hz), which correspond to the long and short period modes, respectively. These frequencies have been used as inputs to Equations 2.3 and 2.4.

The characteristics of the optimal inputs, designed as described in Section 2.2, are presented in Table 3. Δt are the optimal time steps. These values have been calculated with Equations 2.3 and 2.4 for the throttle doublet and short period maneuvers, respectively, and chosen as described in Section 2.2 for the phugoid input. “Maximum amplitude” stands for the highest amplitude of the input to avoid instability and actuator saturation, tested on the model presented by Balmer (2015). The maximum amplitude of the DLR 3211 represents the average absolute amplitude of this signal. The throttle doublet input starts at throttle equal to 0.5, adds up to full throttle, decreases to zero, and returns to 0.5. “Oscillation time” is the minimum time that the aircraft should be allowed to oscillate freely after the maneuver. This value is equivalent to the period of the mode it is intended to excite (see Section 2.2).

For the purpose of this work, the bandwidth of the inputs have been considered to be the range of frequencies that exhibit at least 50% of the maximum energy of the signal. It is assumed that only the dynamics within that range will be excited with sufficient energy to affect the measurements. The analysis of identifiability of the derivatives is carried out by taking into account the magnitude of their terms within the bandwidth of the signals.

Table 3 – Characteristics of optimal elevator and throttle inputs.

Maneuver	$\Delta t(\text{s})$	Maximum amplitude	Oscillation time	Bandwidth
Short period	0.18	0.6 rad	0.81 s	1.76 ~ 15.60 rad/s
Phugoid	1.6	0.18 rad	11.75 s	0 ~ 1.73 rad/s
Throttle doublet	4.29	0.5 ± 0.5	11.75 s	0.27 ~ 0.85 rad/s

Source: The author.

The input signals in the time domain, as well as their power spectra are shown in Figure 9. The frequencies of the modes each maneuver is intended to excite are indicated with arrows.

Since there is no strict requirement on the time step of the long period input, a value of Δt equal to 1.6 seconds was found suitable. Longer time steps easily destabilize the system. To avoid that, the elevator deflection would have to be reduced, which would

significantly lower the energy of the maneuver. Hence, the advantage of having larger energy content in signals with longer Δt described by Jategaonkar (2015) is, in this case, absent. On the other hand, small values of Δt generate signals with energy contents spread over a large range of frequencies, but with very small magnitudes, which may not be enough to properly excite the system (JATEGAONKAR, 2015). In that context, the time step of the phugoid maneuver was chosen such that its bandwidth would not overlap with the bandwidth associated with the short period maneuver.

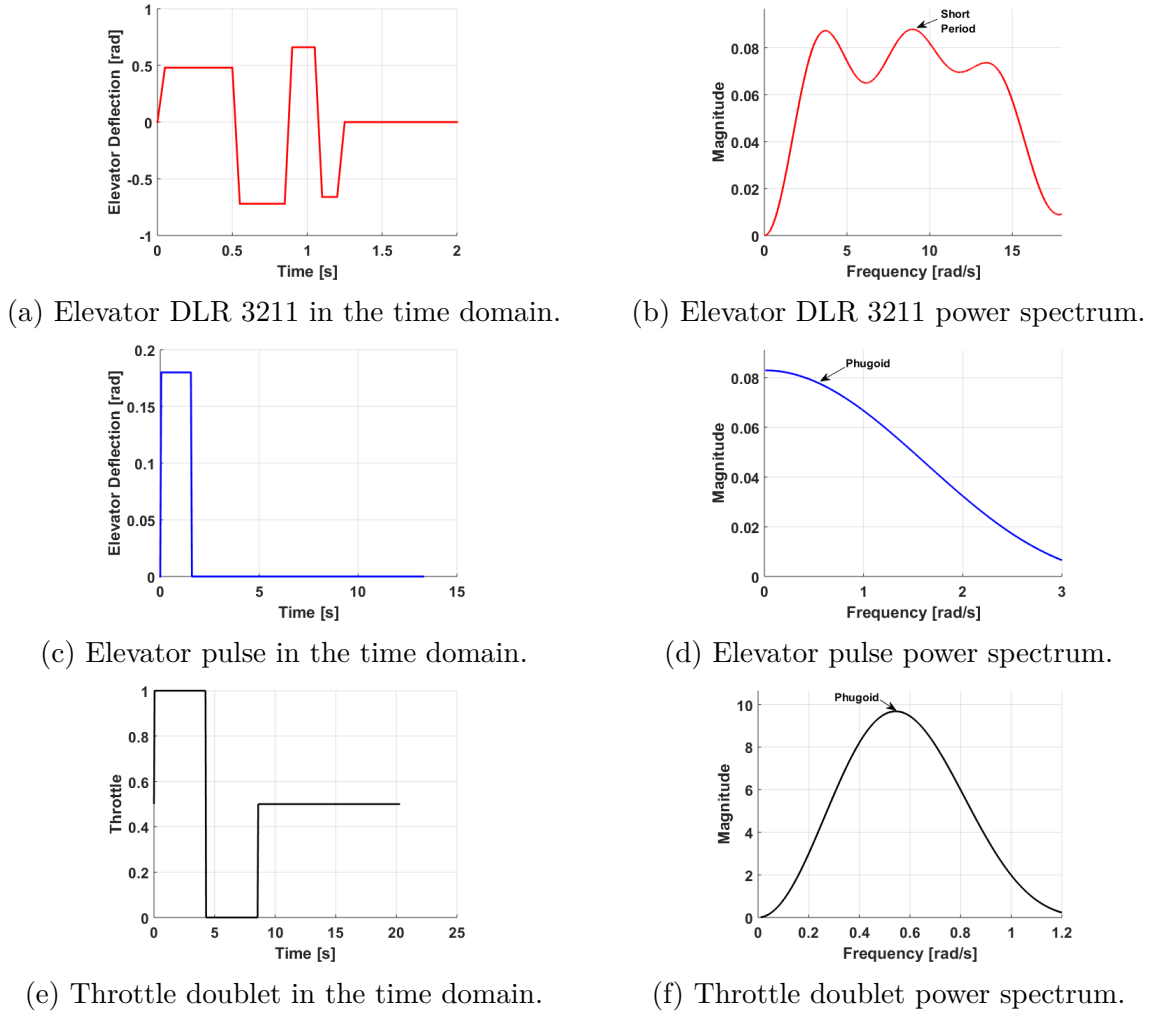


Figure 9 – Optimal inputs in the time and frequency domains.

Source: The author.

Due to time constraints, there has been no possibility of performing maneuvers with the optimal Δt values found using Equations 2.3 and 2.4 in flight tests. Therefore, the available flight data has been used in system identification. The set of inputs performed in the flight tests has been designed by Lee (2017). Instead of centering the maximum energy peak at the eigenfrequencies, Lee defined Δt values such that the bandwidth of the maneuvers would be appropriate to identify all derivatives, except x_{δ_e} , according to the 10% rule. Regarding the number of parameters considered identifiable, both methods have

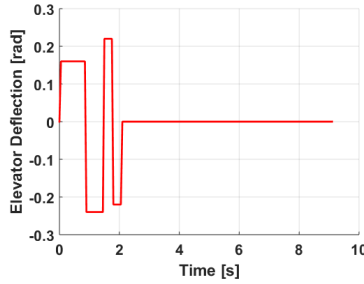
yielded the same results, despite the one presented by Lee (2017) not being concerned about the optimality of the inputs.

Table 4 shows the characteristics of the actual maneuvers performed in flight. The input signals in the time domain, as well as their frequency responses are shown in Figure 10.

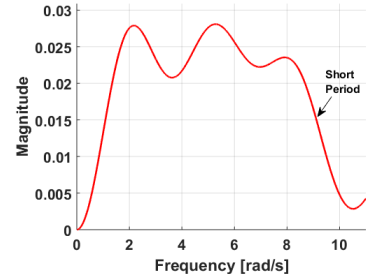
Table 4 – Characteristics of the inputs from flight data.

Maneuver	$\Delta t(s)$	Amplitude	Oscillation time	Bandwidth
Short period	0.3	0.2 rad	~ 7 s	1.04~9.19 rad/s
Phugoid	1	0.2 rad	~ 27 s	0~2.78 rad/s
Throttle doublet	3	0.6 ± 0.4	~ 27 s	0.38~1.22 rad/s

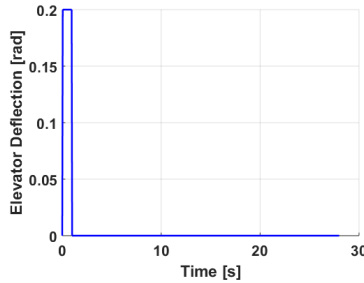
Source: Lee (2017).



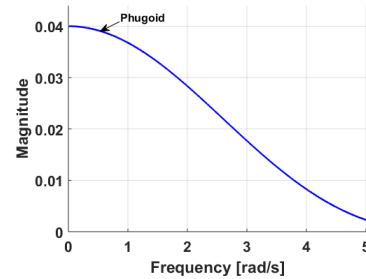
(a) Elevator DLR 3211 in the time domain.



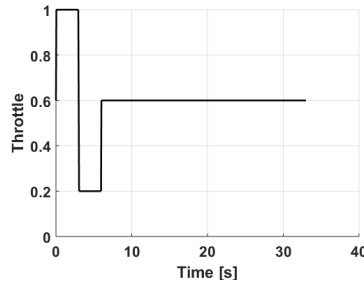
(b) Elevator DLR 3211 power spectrum.



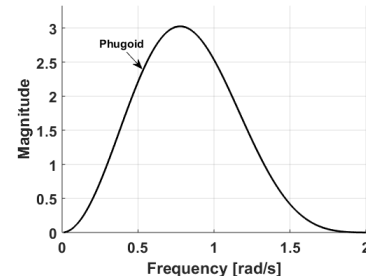
(c) Elevator pulse in the time domain.



(d) Elevator pulse power spectrum.



(e) Throttle doublet in the time domain.



(f) Throttle doublet power spectrum.

Figure 10 – Actual flight data inputs in the time and frequency domains.

Source: The author.

As previously discussed, the time step of the phugoid was chosen such that the input does not excite frequencies already excited by the short period maneuver. However, since

the phugoid mode is lightly damped and requires relatively low energy to be excited, the choice on Δt is somewhat flexible. Hence, a time step of 1 second should yield equivalent results to the one previously selected. In what concerns the throttle doublet maneuver applied, its power spectrum has its peak at about 0.77 rad/s while the natural frequency of the phugoid mode from the *a priori* model is excited with about 79% of the maximum power. Despite not being optimal, this input may also be sufficient since the natural frequency of the mode is within the identifiable bandwidth of the maneuver and reasonably close to its peak. On the other hand, the DLR 3211 maneuver used in the flight test has its peak at about 5.26 rad/s, while the natural frequency of the mode it is intended to excite is located at a point that represents about 56% of the maximum power. Considering that this value is still within the bandwidth, the maneuver is also considered acceptable. Adding to that, it is known that the actual oscillation frequency of damped modes, i.e., their damped natural frequency, is lower than their natural frequency (MILLER; MATTUCK, 2010).

After examining the time steps of the recorded inputs, a frequency domain analysis of the *a priori* model has been performed in order to validate the set of maneuvers, according to the 10% rule. To accomplish that, it is assumed that the linearized longitudinal model of the aircraft is as given in Equation 3.1.

$$\begin{aligned}
 \dot{u} &= x_0 + x_u u + x_w w + x_q q + x_\theta \theta + x_\omega \omega + x_{\delta e} \delta e \\
 \dot{w} &= z_0 + z_u u + z_w w + z_q q + z_\theta \theta + z_{\delta e} \delta e \\
 \dot{q} &= m_0 + m_u u + m_w w + m_q q + m_\omega \omega + m_{\delta e} \delta e \\
 \dot{\theta} &= q \\
 \dot{\omega} &= k_0 + k_u u + k_w w - \frac{1}{T_w} \omega + \frac{k_\omega}{T_w} \delta t
 \end{aligned} \tag{3.1}$$

where x_0 , z_0 , m_0 , and k_0 are biases; x_u , x_w , x_q , x_θ , x_ω , $x_{\delta e}$, z_u , z_w , z_q , z_θ , $z_{\delta e}$, m_u , m_w , m_q , m_ω , and $m_{\delta e}$ are the so called concise derivatives, which have this name because they represent larger expressions involving the aircraft dimensional derivatives. These are adopted for the sake of notation simplicity. The equivalent expressions to the concise derivatives can be found in Cook (2012). k_u , k_w , $\frac{-1}{T_w}$, $\frac{k_\omega}{T_w}$ are engine dynamics components.

The concise derivatives and engine dynamics components are defined in Appendix A. The engine dynamics equation has been assumed to be of this form in order to account for all nonzero components of the fifth line of the *a priori* model (Section 2.1). The Laplace transform of this equation is shown in Appendix A. Furthermore, all the biases are assumed to be zero, and the values of the derivatives have been taken from the *a priori* model.

Bode plots containing each term on the right-hand side of Equation 3.1 have been generated in order to investigate the identifiability of the parameters within the range of each flight test maneuver, according to the 10% rule defined in Section 2.2. The plots can be seen in Figure 11. The Bode diagrams of the derivative terms are generated by

plotting the frequency response magnitude of the terms in Equation 3.1 as a function of the input signal, which for the left-hand-side plots is the elevator command and for the right-hand-side figures is the throttle command.

To demonstrate the procedure applied, axial force equation is considered. The frequency response magnitudes of each of the terms, namely x_u , x_w , x_q , x_θ , x_ω , and $x_{\delta e}$, are plotted with respect to the elevator input. The magnitudes being computed in this case are shown in Equation 3.2.

$$\left| \frac{x_u u(\omega)}{\delta e(\omega)} \right|, \left| \frac{x_w w(\omega)}{\delta e(\omega)} \right|, \left| \frac{x_q q(\omega)}{\delta e(\omega)} \right|, \left| \frac{x_\theta \theta(\omega)}{\delta e(\omega)} \right|, \left| \frac{x_\omega \omega(\omega)}{\delta e(\omega)} \right|, \left| \frac{x_{\delta e} \delta e(\omega)}{\delta e(\omega)} \right| \quad (3.2)$$

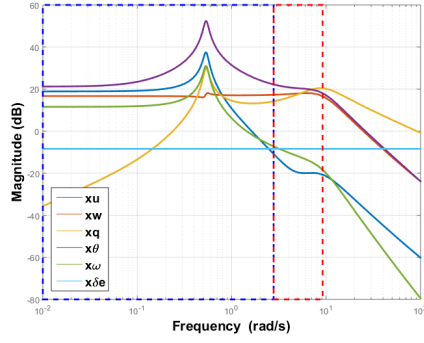
where argument (ω) denotes the Fourier transform of the variables.

The individual components are then computed from the output equation $y = C[u \ w \ q \ \theta \ \omega]^T + D\delta e$, with the observation matrices C and D defined as shown in Equation 3.3. The values of the vectors are taken from the *a priori* model. The subscripts denote the observation matrices for the corresponding components.

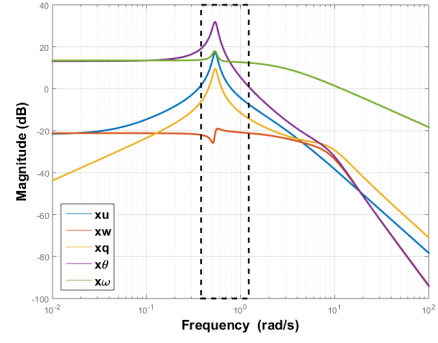
$$\begin{aligned} C_u &= [-0.10 \ 0 \ 0 \ 0 \ 0], \ D_u = [0] \\ C_w &= [0 \ 0.39 \ 0 \ 0 \ 0], \ D_w = [0] \\ C_q &= [0 \ 0 \ -1.4 \ 0 \ 0], \ D_q = [0] \\ C_\theta &= [0 \ 0 \ 0 \ -9.8 \ 0], \ D_\theta = [0] \\ C_\omega &= [0 \ 0 \ 0 \ 0 \ 0.006], \ D_\omega = [0] \\ C_{\delta e} &= [0 \ 0 \ 0 \ 0 \ 0], \ D_{\delta e} = [0.38] \end{aligned} \quad (3.3)$$

The same procedure has been performed for throttle as input and for all other equations, except the one for θ since the first derivative of this variable is considered to be equal to q . Consequently, there are no parameters to be identified in this equation.

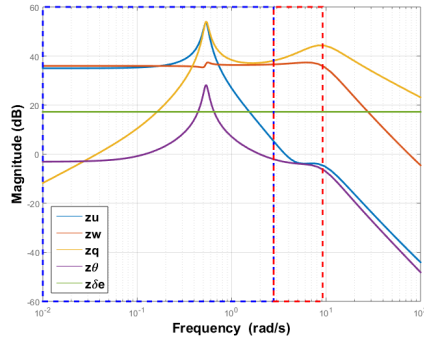
The blue, red and black dashed boxes shown in the Bode plots delimit the regions of identifiability of phugoid, short period and throttle doublet maneuvers, respectively. In addition to the identifiability analysis, a study of the best input to identify each derivative is also performed by analyzing the maximum magnitude of a term compared to the other terms within the maneuver range. In order to avoid overlapping and make the choice clearer, the left edge of the bandwidth of the short-period input was defined to start at the right cutoff frequency of the phugoid maneuver. Since all frequencies in the bandwidth of the inputs are excited, the investigation is carried out by comparing the maximum magnitude of all terms within that range, even if the maximum values do not happen at the same frequency. The results of this analysis are shown in Table 5.



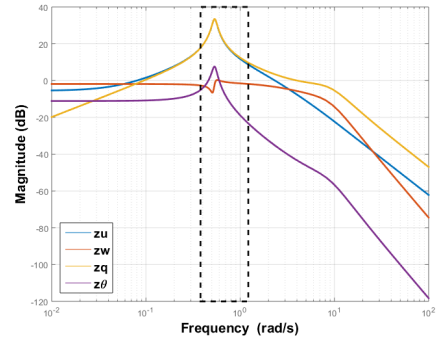
(a) Axial force terms. Elevator as input.



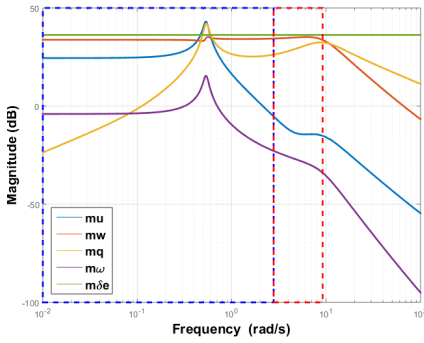
(b) Axial force terms. Throttle as input.



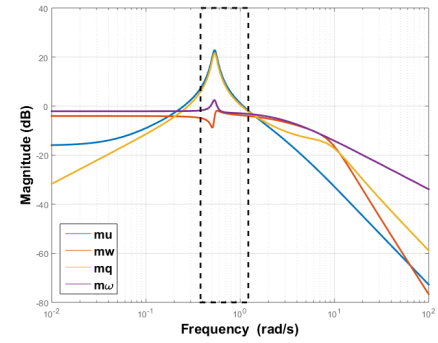
(c) Normal force terms. Elevator as input.



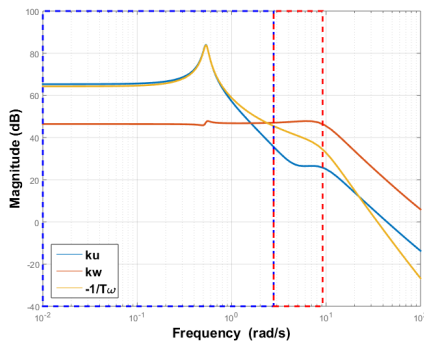
(d) Normal force terms. Throttle as input.



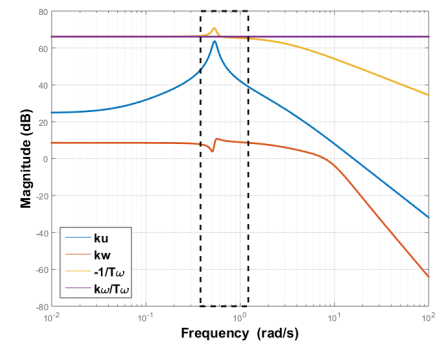
(e) Pitching moment terms. Elevator as input.



(f) Pitching moment terms. Throttle as input.



(g) Engine dynamics terms. Elevator as input.



(h) Engine dynamics terms. Throttle as input.

Figure 11 – Bode plots of derivative terms. The blue, red, and black dashed rectangles represent the regions of identifiability of the phugoid, short period, and throttle doublet maneuvers, respectively.

Source: The author.

In order to clarify the choice on the best maneuver to identify each derivative the analysis of the m_u term, from Figure 11 (e) and (f), is explained.

In the throttle doublet maneuver range, m_u exhibits a maximum magnitude of 22.9 dB, in contrast with the maximum values of the other terms, which are 21.7 dB, 2.54 dB and -1.91 dB.

In the bandwidth of the phugoid input, the maximum magnitude of m_u is 42.5 dB, while the other terms have maximum peaks of 42.2 dB, 36.3 dB, 35.2 dB and 15.6 dB.

Analyzing the short period maneuver identifiability range, it can be seen that the m_u term has a maximum magnitude of -6.09 dB, while the other terms exhibit maximum values of 36.3 dB, 34.9 dB, 32.5 dB and -22.8 dB.

From this analysis it can be concluded that the term m_u is best identified using the throttle doublet maneuver since its relative maximum magnitude compared to the other terms is greater than the ones exhibited in the ranges of the other two inputs. Besides that the term can be considered identifiable in the phugoid range and not identifiable within the short period bandwidth.

Furthermore, it can be noticed that the terms related to the parameters present in the B matrix from the state-space model represent straight lines in the Bode diagrams. This occurs due to the fact that these terms are static. It can be also noticed from Equation 3.2 that the variables that multiply these parameters are canceled out.

Table 5 – Identifiability of derivatives.

Derivative	Phugoid	Short period	Throttle doublet
x_u	Best.	Not identifiable.	Identifiable.
x_w	Identifiable.	Best.	Not identifiable.
x_q	Identifiable.	Best.	Identifiable.
x_θ	Identifiable.	Identifiable.	Best.
x_ω	Identifiable.	Not identifiable.	Best.
$x_{\delta e}$	Not identifiable.	Not identifiable.	Not identifiable.
z_u	Identifiable.	Identifiable.	Best.
z_w	Identifiable.	Best.	Not identifiable.
z_q	Identifiable.	Best.	Identifiable.
z_θ	Best.	Not identifiable.	Identifiable.
$z_{\delta e}$	Identifiable.	Best.	Not identifiable.
m_u	Identifiable.	Not identifiable.	Best.
m_w	Identifiable.	Best.	Not identifiable.
m_q	Identifiable.	Identifiable.	Best.
m_ω	Best.	Not identifiable.	Identifiable.
$m_{\delta e}$	Identifiable.	Best.	Not identifiable.
k_u	Best.	Identifiable.	Identifiable.
k_w	Identifiable.	Best.	Identifiable.
$-\frac{1}{T_\omega}$	Identifiable.	Best.	Identifiable.
$\frac{k_\omega}{T_\omega}$	Not identifiable.	Not identifiable.	Best.

Source: The author.

According to the examination of the magnitude of the terms, all parameters except

x_{δ_e} can be identified using the flight data. It can be also concluded that the use of all kinds of maneuvers would possibly yield better results since the largest relative magnitude of the terms are distributed over the three ranges. In addition, the use of different inputs is also beneficial for the robustness of the parameter estimation, avoiding a possible limited operating range of the model.

From the available flight test data, three maneuvers of each kind have been chosen for the identification procedure. Since an autopilot has been used, all inputs have been adequately performed in terms of amplitude and time step; however in a few of them, enough time for the aircraft to oscillate has not been given. Those maneuvers have been discarded.

From the set of nine maneuvers considered useful, one of each class has been randomly chosen to compose the validation set, which has not been used during identification. Therefore, a total of six maneuvers have been used for identification and three maneuvers have been adopted for the validation procedure. Figures 12 and 13 display the inputs of the identification and validation sets, respectively. The vertical black lines delimit the maneuvers.

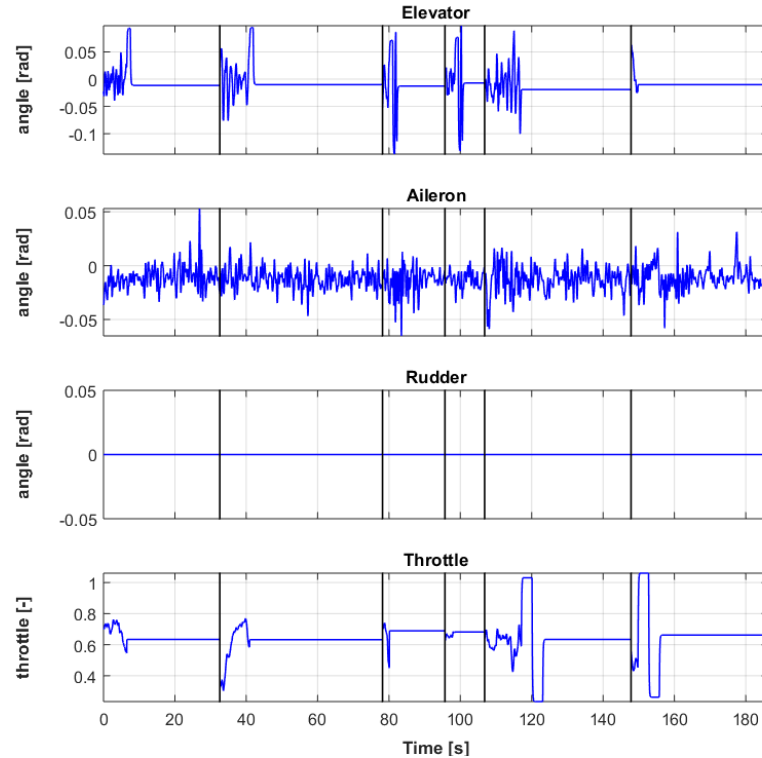


Figure 12 – Inputs used in identification.

Source: The author.

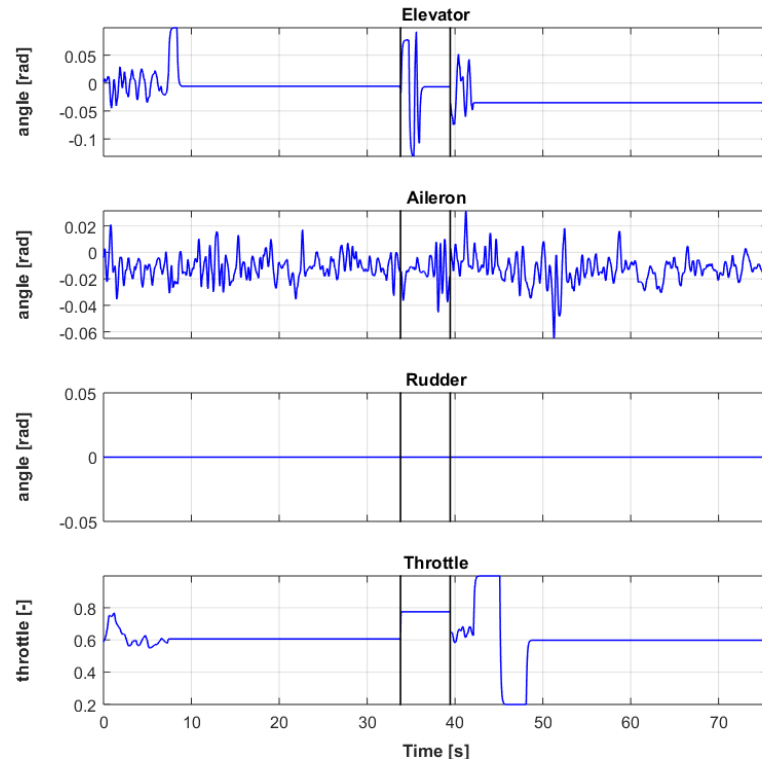


Figure 13 – Inputs used in validation.

Source: The author.

3.2 System identification results

3.2.1 Results of the *a priori* model

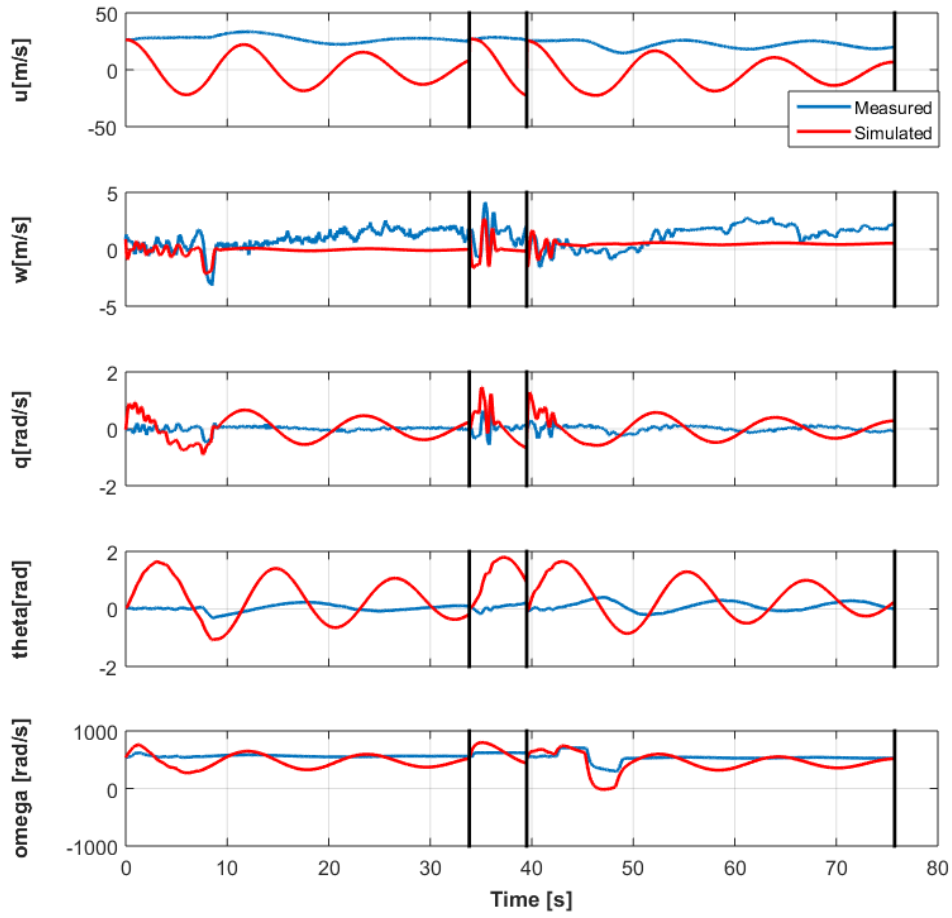
The states generated by the application of the validation maneuvers to the *a priori* state-space model, presented in Section 2.1, are shown in Figure 14. The states simulated with the *a priori* model are plotted in red. The measured states are shown in blue.

Tables 6 and 7 present Goodness of Fit and Theil's inequality coefficients, which compare the simulation results and the measurements of the states from the identification and validation sets, respectively.

Table 6 – Statistical measures of the states simulated using the *a priori* model – identification set.

Measure	u	w	q	θ	ω
GOF	-88.6034	-1.1008	-13.4752	-50.4809	-6.5016
TIC	0.7384	0.7517	0.7793	0.8340	0.1149

Source: The author.

Figure 14 – States simulated with the *a priori* model and measured states.

Source: The author.

Table 7 – Statistical measures of the states simulated using the *a priori* model – validation set.

Measure	u	w	q	θ	ω
GOF	-49.6545	-0.6371	-12.0559	-34.1344	-4.8069
TIC	0.7466	0.6332	0.7864	0.8222	0.1309

Source: The author.

By analyzing Figure 14 and Tables 6 and 7 it can be concluded that the *a priori* model does not sufficiently simulate the aircraft behavior. Due to that, an effort to identify a new model by applying the Output Error and Two Step methods has been found necessary.

3.2.2 Results of the Output Error Method

The application of the Output Error Method resulted in the state-space model shown in Equation 3.4. The state and measurement bias vectors are shown in Equation 3.5. Figure 15 presents a comparison between the time series of the measured and simulated

states. The latter are shown in red. These were generated through the integration of the left-hand side of the state equation (Eq. 3.1), with the validation set of maneuvers (Fig. 13) as inputs. The measured states are plotted in blue.

$$\begin{bmatrix} \dot{u} \\ \dot{w} \\ \dot{q} \\ \dot{\theta} \\ \dot{\omega} \end{bmatrix} = \begin{bmatrix} -0.1122 & 1.143 & -2.1000 & -13.17 & 0.005679 \\ -0.6331 & -2.860 & 22.02 & -1.768 & 0 \\ -0.008642 & -0.5316 & -3.663 & 0 & 0.002205 \\ 0 & 0 & 1 & 0 & 0 \\ 5.401 & -7.337 & 0 & 0 & -2.480 \end{bmatrix} \begin{bmatrix} u \\ w \\ q \\ \theta \\ \omega \end{bmatrix} + \begin{bmatrix} 0.38 & 0 \\ -37.13 & 0 \\ -27.81 & 0 \\ 0 & 0 \\ 0 & 1053 \end{bmatrix} \begin{bmatrix} \delta_e \\ \delta_t \end{bmatrix} \quad (3.4)$$

$$\mathbf{b}_x = \begin{bmatrix} -0.3756 \\ 16.3994 \\ -0.8661 \\ -0.05254 \\ 655.4412 \end{bmatrix}, \quad \mathbf{b}_y = \begin{bmatrix} -1.1256 \\ 0.6713 \\ -0.05218 \\ 0.0093 \\ -35.3798 \end{bmatrix} \quad (3.5)$$

The GOF and TIC measures for both identification and validation sets are shown in Tables 8 and 9, respectively.

Table 8 – Statistical measures of the states resulting from the Output Error Method – identification set.

Measure	\mathbf{u}	\mathbf{w}	\mathbf{q}	$\boldsymbol{\theta}$	$\boldsymbol{\omega}$
GOF	0.6604	0.3876	0.7225	0.7669	0.9363
TIC	0.0347	0.2737	0.2861	0.2222	0.0102

Source: The author.

Table 9 – Statistical measures of the states resulting from the Output Error Method – validation set.

Measure	\mathbf{u}	\mathbf{w}	\mathbf{q}	$\boldsymbol{\theta}$	$\boldsymbol{\omega}$
GOF	0.7366	-0.4452	0.6843	0.5399	0.9156
TIC	0.0424	0.3514	0.3080	0.2879	0.0152

Source: The author.

The GOF values of w suggest poor matching between measurements and estimates in both, identification and validation. The negative value in the latter suggests that a straight line would fit flight data better than the model prediction. However, the TIC measure indicates that the match for this state, in validation, is reasonably close to the 0.3 threshold, mentioned in Section 2.5, although being above it. A probable cause for that is a possible inaccuracy of the GPS to acquire altitude variations.

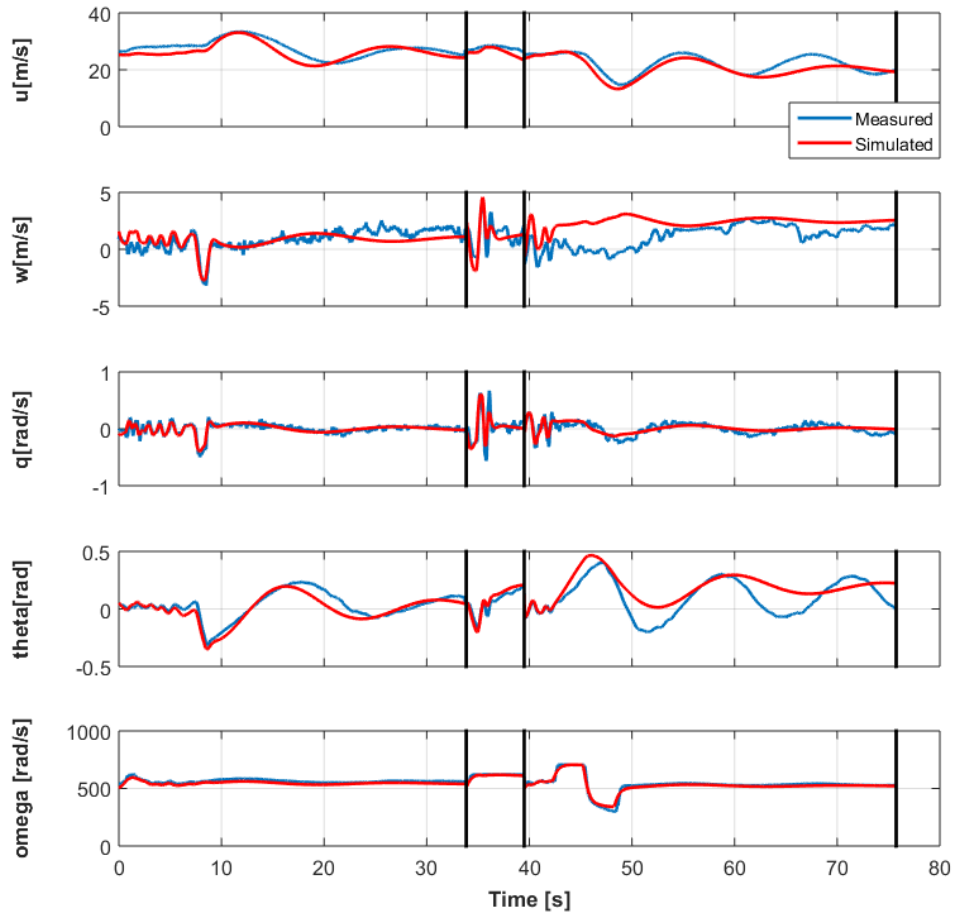


Figure 15 – States simulated with the model resulting from the Output Error Method and measured states.

Source: The author.

In the validation set of θ , the TIC measure exhibits a value of 0.3080. This value is slightly higher than the limit of reasonable agreement between the data. Nevertheless, this deviation may not constrain control design.

The model prediction capacity for the other states is satisfactory, with ω exhibiting the best fit. This may have occurred due to the fact that no scaling or normalization is present in the error covariance matrix, R , presented in Equation 2.8 or in the cost function, shown in Equation 2.9. This induces the optimization algorithm to minimize variables that exhibit higher values to the detriment of those with lower magnitudes, as long as the cost function is reduced.

An overall worse match in the throttle doublet maneuver for all states, except ω , may also indicate that adding the state ω to the state-space model, in order to account for the engine dynamics, does not exclude the necessity of having a proper throttle-thrust mapping if a closer fit is desired.

The identified state-space system has the following poles

Phugoid:	$-0.07331 \pm 0.4256j$
Short period:	$-3.2166 \pm 3.4474j$
Engine dynamics:	-2.5354

Compared to the *a priori* model, the identified long and short period modes present lower oscillation frequency. The former exhibits higher and the latter, lower damping. The identified engine dynamics time constant is slightly higher than the one previously found.

3.2.3 Results of the Two Step Method

This section is divided in two parts, which concern the presentation of the results of flight path reconstruction and the parameter estimation procedures, respectively.

3.2.3.1 Flight path reconstruction results

The first part of the Two Step Method yields an estimation of the biases present in the linear acceleration and angular rate measurements. As described in Section 2.4.1, the variables recorded in flight are used as inputs to the rigid-body 6DOF kinematic equations, shown in Equation 2.10. Then, an estimation of the bias values is carried out in order to minimize the errors between the time series of the measured states and the ones resulting from the integration of the 6DOF kinematic equations with biases included.

The predicted states from the validation set with biases resulting from maximum likelihood estimation are plotted in Figure 16 together with the measurements. The values of the estimated biases for each maneuver are presented in Table 10.

Table 10 – Estimated measurement biases for each maneuver.

Bias	Phugoid	Short period	Throttle doublet
Δa_x	-9.409×10^{-2}	3.318×10^{-2}	2.650×10^{-1}
Δa_y	-1.511×10^{-1}	-3.422×10^{-1}	-2.666×10^{-2}
Δa_z	-3.447×10^{-3}	-7.690×10^{-2}	-2.797×10^{-2}
Δp	-3.233×10^{-4}	-3.070×10^{-3}	-8.556×10^{-4}
Δq	-3.025×10^{-4}	3.437×10^{-3}	-4.018×10^{-4}
Δr	8.466×10^{-3}	5.642×10^{-3}	3.134×10^{-3}

Source: The author.

It can be noted that biases of the same nature presented different dimensions and even different signs, which justifies the adoption of distinct estimates for each maneuver.

Table 11 shows the statistical measures of the conducted flight path reconstruction.

The overall procedure yielded satisfactory bias estimates. The match between measured and simulated vertical velocity, w , was again the poorest one; however, with a TIC of 0.20823, the agreement between the data is still considered reasonable, according to the criterion presented in Section 2.5.

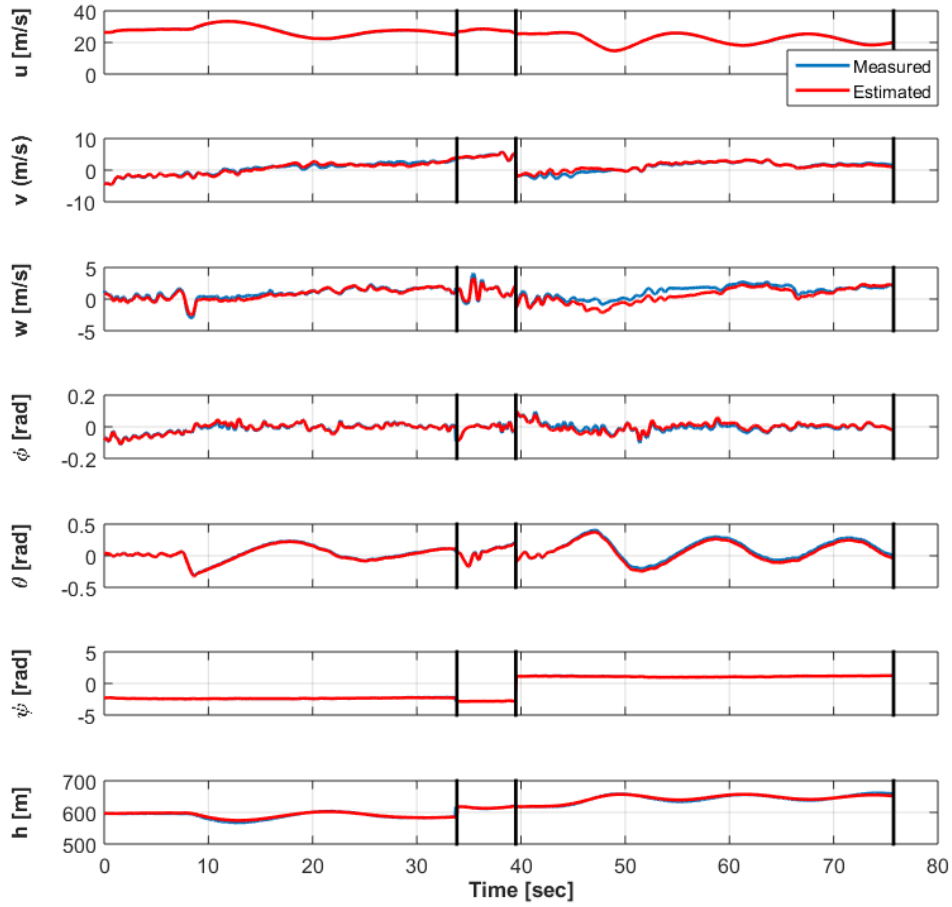


Figure 16 – Measured longitudinal and lateral states and states generated from the integration of the 6DOF equations of motion with estimated biases added.

Source: The author.

Table 11 – Statistical measures of the reconstructed states – validation set.

Measure	u	v	w	ϕ	θ	ψ	h
GOF	0.99879	0.93625	0.6556	0.8488	0.96966	0.99974	0.98777
TIC	0.002799	0.11376	0.20823	0.18542	0.08097	0.007471	0.002550

Source: The author.

3.2.3.2 Results of force and moment components identification

Once acceptable values for biases had been found, an estimate of the actual forces and moments acting in the aircraft during flight could be obtained and a linear regression to find their composing terms has been performed.

The force and moment components, from the right-hand-side of Equation 2.11, estimated through this procedure are shown in Table 12. In Figure 17 the reconstructed forces and moments, as well as the ones resulting from the linear regression are shown. Tables 13 and 14 present the values of the statistical measures for the identification and validation sets, respectively.

Table 12 – Linear regression terms and respective values.

Term	Value	Term	Value	Term	Value
X_0	24.8912	Z_0	-60.0449	M_0	-1.6648
X_u	-1.9521	Z_u	-4.2001	M_u	0.06910
X_w	1.9181	Z_w	-10.8758	M_w	-0.4797
X_q	-1.5002	Z_q	-170.2218	M_q	-7.4845
$X_{\delta e}$	-22.0493	$Z_{\delta e}$	28.5036	$M_{\delta e}$	-55.9172
$X_{\delta t}$	44.7413				

Source: The author.

Table 13 – Statistical measures of the Two Step Method estimated forces and moments – identification set.

Measure	X	Z	M
R^2	0.7609	0.6232	0.4831
RMSE	4.5079	20.3579	0.9393
NRMSE	0.08668	0.06067	0.04044

Source: The author.

Table 14 – Statistical measures of the Two Step Method estimated forces and moments – validation set.

Measure	X	Z	M
R^2	0.7524	0.6593	0.03696
RMSE	4.6814	22.2496	1.2930
NRMSE	0.09414	0.06072	0.05926

Source: The author.

The linear regression plots and statistics indicate that the procedure has yielded acceptable fits, which means that, for this application, forces and moments can be satisfactorily described by a linear combination of longitudinal states, presented in Equation 2.11.

Tables 15 and 16 present the statistical measures of the forces and moments obtained by Lee (2017). As mentioned in Section 2.4, Lee has also performed Two Step system identification for Penguin BE. Nonetheless, that author has performed flight path reconstruction using a stochastic approach, based on an Extended Kalman Filter. In the second step, this work and Lee (2017) have followed the same procedure.

Table 15 – Statistical measures of the Two Step Method forces and moments obtained by Lee (2017) – identification set.

Measure	X	Z	M
R^2	0.868	0.616	0.422
RMSE	3.109	19.779	1.0899
NRMSE	0.071	0.067	0.045

Source: Lee (2017).

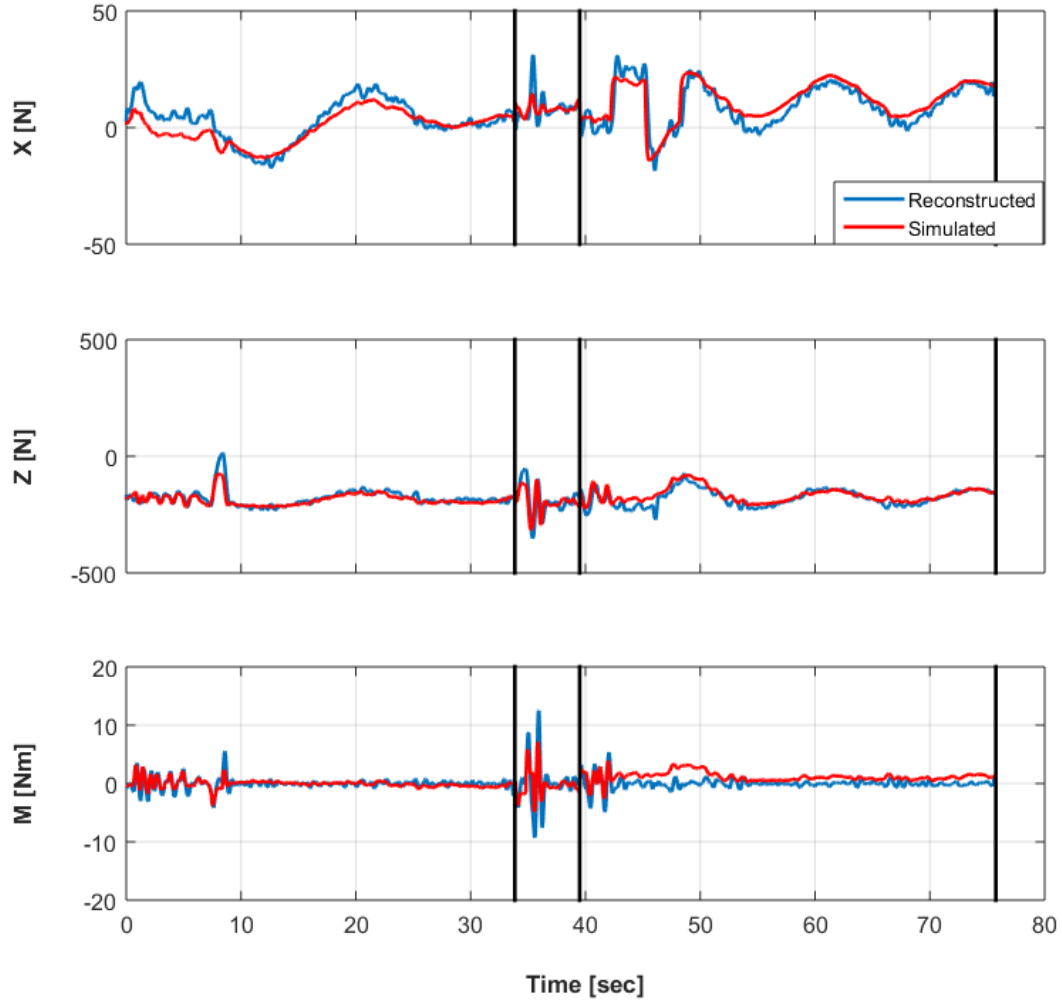


Figure 17 – Reconstructed forces and moments, and forces and moments from linear-regression – validation set.

Source: The author.

Table 16 – Statistical measures of the Two Step Method forces and moments obtained by Lee (2017) – validation set.

Measure	X	Z	M
R^2	0.848	0.665	0.1359
RMSE	4.10	20.63	1.239
NRMSE	0.078	0.067	0.053

Source: Lee (2017).

The statistical measures suggest comparable estimates of Z and M with the ones obtained by Lee (2017). Nevertheless, the estimation of X carried out by Lee (2017) seem to have yielded more reliable results.

The longitudinal states have been generated through the application of the estimated forces and moments in the longitudinal 6DOF dynamic equations, with measurements

of the lateral states and the lateral angular rates corrected with the estimated biases included, as shown in Equation 2.12.

The longitudinal states generated from the integration of the 6DOF dynamic equations, along with the measurements are plotted in Figure 18. The GOF and TIC statistical indicators of performance for the identification and validation sets are shown in Tables 17 and 18, respectively.

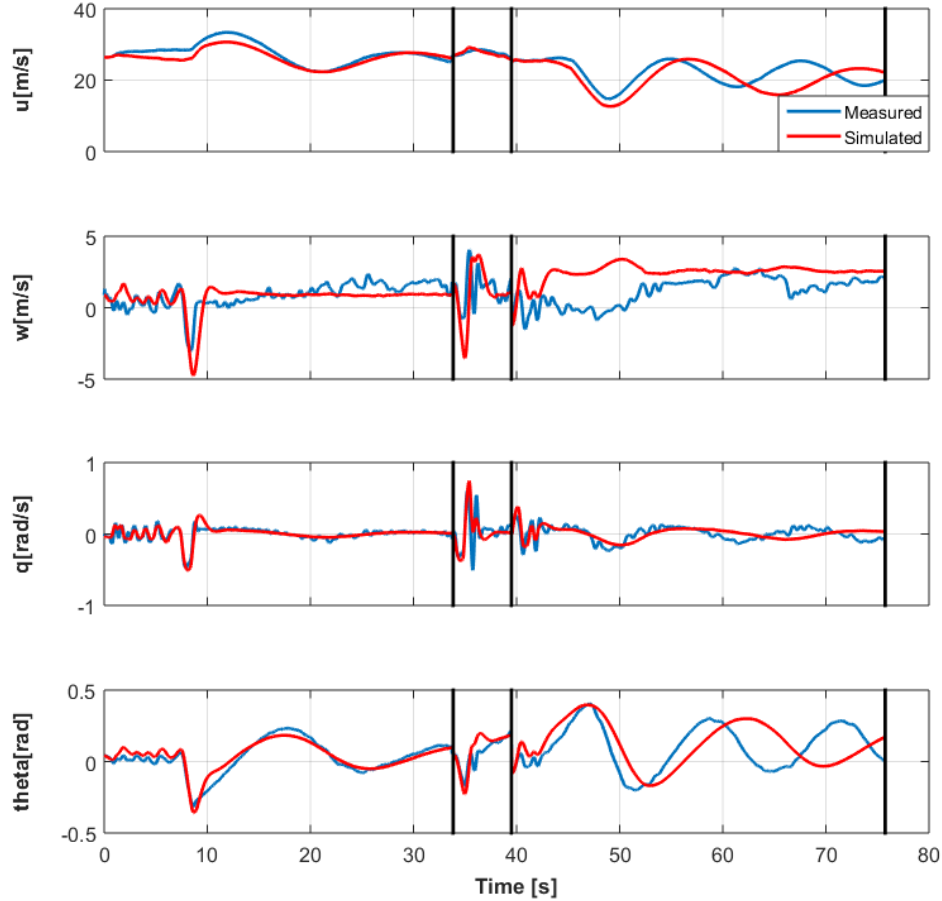


Figure 18 – Measured and Two Step Method simulated states.

Source: The author.

Table 17 – Statistical measures of the states resulting from the Two Step Method – identification set.

Measure	u	w	q	θ
GOF	0.3680	0.1027	0.5069	0.3745
TIC	0.04729	0.3101	0.3423	0.3437

Source: The author.

The states w , q , and θ , generated by the integration of the 6DOF dynamic equations, present GOF measures below 0.5 in the validation set, which is possibly due to a frequency mismatch in the data from the throttle doublet maneuver. The TIC indicators for the

Table 18 – Statistical measures of the states resulting from the Two Step Method – validation set.

Measure	u	w	q	θ
GOF	0.5330	-1.0559	0.4331	0.3207
TIC	0.05612	0.3979	0.3833	0.3688

Source: The author.

same variables are above 0.3 for both identification and validation, which suggest deficient agreement between the data. Regarding the linear velocity u , TIC and GOF seem to indicate satisfactory estimation. Despite the latter not being much close to one, the former is well below 0.3. The difference between the measurements and estimates of this state in the first seconds may be due to a mismatch on the estimate of the aircraft axial force, X , within the same range.

Except by w , which has presented overall insufficient estimates in this technique, the other states seem to match the measured data appropriately for the phugoid and short period maneuvers. The frequency mismatch and phase shift exhibited in the throttle doublet maneuver may possibly have occurred due to the fact that engine dynamics have not been taken into account in the Two Step Method. A possible solution would be adding the state ω to the linear expressions of the forces and moments, similarly to what has been performed in the state equations in the Output Error Method. Another possibility would be estimating the aerodynamic forces and moments apart from the propulsion ones.

Tables 19 and 20 present the GOF and TIC measures for the states obtained by Lee (2017). Identification and validation sets are shown.

Table 19 – Statistical measures of the Two Step Method states obtained by Lee (2017) – identification set.

Measure	u	w	q	θ
GOF	0.3680	0.1027	0.5069	0.3745
TIC	0.04729	0.3101	0.3423	0.3437

Source: The author.

Table 20 – Statistical measures of the Two Step Method states obtained by Lee (2017) – validation set.

Measure	u	w	q	θ
GOF	0.5330	-1.0559	0.4331	0.3207
TIC	0.05612	0.3979	0.3833	0.3688

Source: The author.

Except by the TIC values of q in the identification set and w in the validation set all other statistical measures suggest that the stochastic approach performed by Lee (2017)

has yielded better results than the deterministic one adopted in this work for the Two Step Method.

3.2.4 Comparison between identification methods

Figure 19 shows measurements (in blue) and states resulting from the Output Error (in red) and Two Step (in green) methods from the validation set of maneuvers. It is possible to note that estimates of w from the Output Error approach seem to match the flight data more closely than the ones provided by the Two Step Method. The other states have reasonably similar results in the first two maneuvers, with OEM yielding slightly more accurate results in the third one.

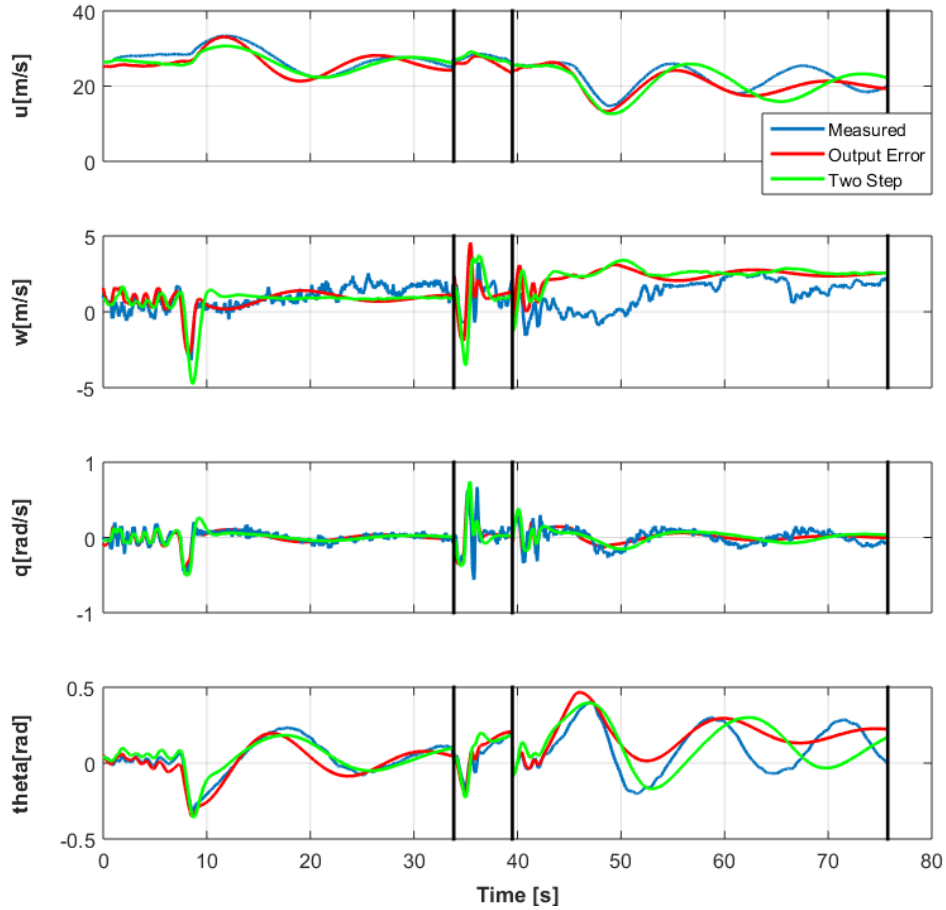


Figure 19 – Measured States and states resulting from the Output Error and Two Step identified models.

Source: The author.

The statistical indicators suggest that the system identification performed using the Output Error Method has yielded overall better results than the Two Step Method. A possible cause is the inclusion of the engine dynamics on the state-space model identified by the former. As mentioned in Section 3.2.3.2, adding the motor angular velocity, ω , to

the linear expressions of the forces and moments or identifying separate aerodynamic and propulsion equations could possibly yield more adequate results for the Two Step Method.

The lack of a proper throttle-thrust mapping and the consequent adoption of the throttle command as an input to the model has proven to be a jeopardizing factor for the achievement of better results. When engine dynamics are not included an instantaneous relationship between throttle command and state variation is usually assumed. This causes the effects of thrust variations in the model to instantly happen when the throttle command is perturbed, which, on the actual aircraft, goes through a phase lag before it can be noticed by the sensors. The use of motor angular velocity ω seem to have slightly improved the match between the model and the real aircraft dynamics and can be considered as a solution in the absence of such mapping. Another possible reason to the mismatch, mentioned by Lee (2017), is that the fact that the states in the Output Error Method and the forces and moments in the Two Step approach have only linear first order terms may have caused inaccurate estimates, especially in the throttle doublet maneuver.

Besides that, it is possible to note that the throttle doublet maneuver has generated oscillations with larger amplitudes in θ . This may have caused the system to move out of the region of linearity. The maximum amplitude of the maneuvers that keep the system inside that region has not been taken into account in the optimal input design process. However, in future experiments throttle doublets with lower amplitudes will be tested.

Furthermore, the non inclusion of elevator dynamics also appear to have caused some phase shift and could be corrected by the addition of a mapping relating pilot command and actual surface deflection. Moreover, the estimates of w are not satisfactorily accurate, which may be due to possible GPS inaccuracies in measuring this state.

Adding to that, the fact that the Output Error Method has yielded an adequate linear model, in contrast with the nonlinear results of the Two Step method from both, this work and Lee (2017), makes it a more attractive choice for control design. Linear equations to represent the aircraft dynamics could also be generated by linearizing the models resulting from the Two Step Method. Nevertheless, no adequate linear representation could be found by applying such procedure. In fact, it seems to be a more reasonable choice to identify the parameters of a linear model directly, instead of performing identification of a nonlinear one and then linearizing it. The inaccuracies present in the nonlinear model seem to be aggravated when the linearization procedure is carried out.

Although multiple techniques have been developed within aircraft nonlinear control field, like Backstepping (HARKEGARD; GLAD, 2007), those are mostly applied in case a linear model of the vehicle does not present adequate results. In this case, however, the linear model identified using the Output Error Method will be utilized.

3.3 Results of Parameter Space Control Design

The application of a step input to the system formed by the in-flight-tuned controller and the identified model exhibited the following characteristics.

Table 21 – Performance indicators of the actual control system.

Overshoot	Settling time	Rise time
1.69 %	9.87 s	0.97 s

Source: The author.

Figure 20 presents the results of the parameter space analysis of multiple control designs around the currently utilized gains, presented in Section 2.6. The figures show scatter plots of the values of the gains in combinations of two elements. In the left-side figures, the circles of different sizes and colors refer to the predefined stability and performance specifications, namely stable system (yellow), overshoot less than 5% (blue), settling time (5% criterion) less than 10 seconds (green), and rise time less than 1 second (red). In these figures, a circle plotted at a pair of gains means that the system fulfills the specification represented by its color for those two gains and some value of the third gain, which is not included in the plot. In the figures on the right, black circles are plotted where the set of gains fulfilled all the requirements at the same time.

The divergence between the intersections of all colors on the left and the black areas on the right-hand-side plots are due to the fact that, on the left plots, if circles of more than one color are present at a point, it is possible that the requirements have been fulfilled for different values of the third gain that is not plotted. For instance, the overshoot requirement may have been fulfilled for $K_\theta = 1$, $K_{i\theta} = 0.2 \text{ seconds}^{-1}$, and $K_q = 0.3 \text{ seconds}$, and the settling time specification may have been met for $K_\theta = 1$, $K_{i\theta} = 0.2 \text{ seconds}^{-1}$, and $K_q = 0.1 \text{ seconds}$. In this situation, although the two requirements have been fulfilled for different values of K_q , a blue circle and a green one will be plotted at the point $[1; 0.2]$ in the plot of $K_\theta \times K_{i\theta}$ since it does not take the value of K_q into account. On the other hand, only the points where all the specifications have been met at the same time are marked with a circle in the figures on the right.

The gains that are currently in use in flight experiments are represented on the left and right-hand-side plots by black and green circles, respectively. Figure 21 is a three-dimensional plot of the region where all specifications are satisfied. It can be interpreted as a combination of the three figures on the right-hand side of Figure 20.

All sets of gains tested keep the system stable, although yellow circles cannot be clearly seen in some regions of the figures on the left.

It is possible to note that the gains currently used in the aircraft's current autopilot fall inside the region formed by the specifications, which is a possible indicator that the

model is suitable for control design. Assuming that the identified plant perfectly matches the real one, any set of gains that fall inside the black regions could be chosen in order to meet the requirements.

The parameter space analysis also gives an insight of which characteristics are improved or worsened, if the gains are increased or decreased. In the left-side figures in Figure 20, it can be noted that decreasing $K_{i\theta}$ would increase the settling time. On the other hand, if the same gain is increased, the percentage of overshoot starts to get larger. From the same examination, one may conclude that excessively increasing K_q makes the system's rise time exceed the maximum value specified. Small K_θ may also worsen settling time for some values of $K_{i\theta}$. Nevertheless, actuator saturations that may occur for large values of that gain should also be accounted for. In this case, however, since the range of K_θ adopted is relatively small, saturation effects have not been taken into account.

From this analysis, other sets of gains with better performance could be chosen, in case the actual ones are unsatisfactory. An example would be $K_\theta = 1$, $K_{i\theta} = 0.12$ seconds⁻¹, and $K_q = 0.18$ seconds, which, when applied to the identified plant, exhibits the following characteristics: overshoot of 0.88%, settling time of 1.37 seconds, and rise time of 0.97 seconds.

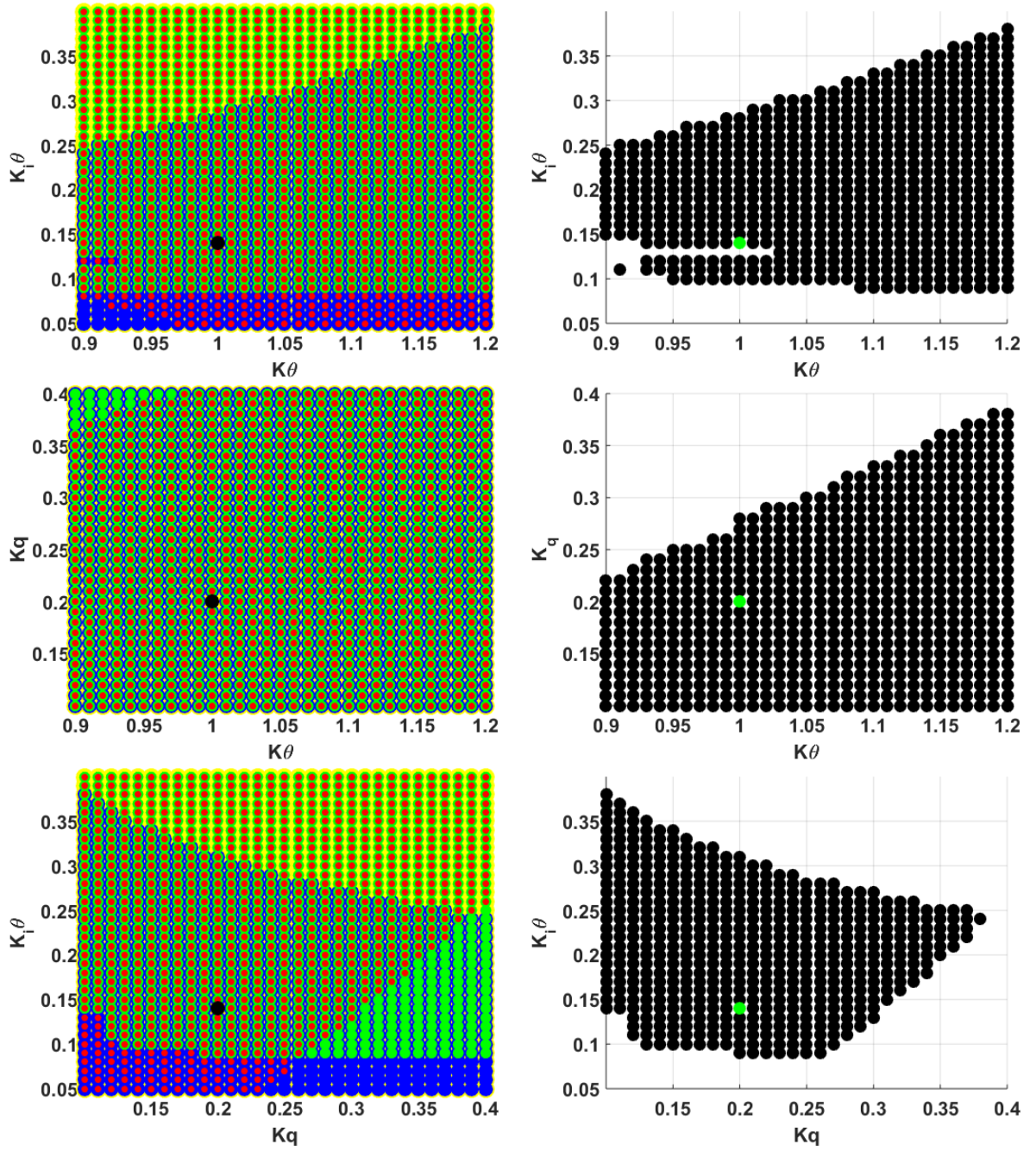


Figure 20 – System performance in the parameter space. All specification regions on the left. Intersection of specifications on the right. Left-hand-side plots: yellow – stable system; blue – overshoot less than 5%; green – settling time less than 10 seconds; red – rise time less than 1 second; black – gains currently in use. Right-hand-side plots: black – gains where all specifications are met at the same time; green – gains currently in use.

Source: The author.

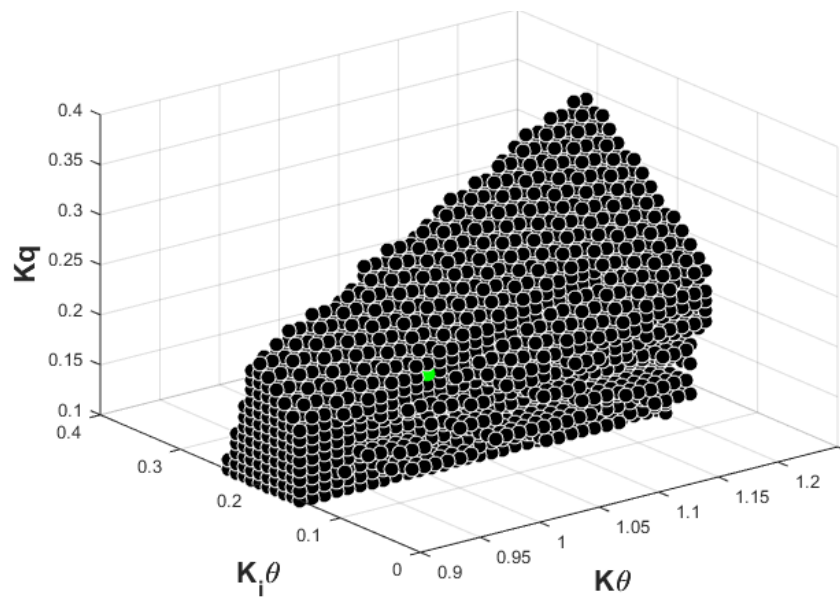


Figure 21 – Intersection of specifications in the three-dimensional parameter space. Black spheres – gains where all specifications are met at the same time; green sphere – gains currently in use

Source: The author.

4 CONCLUSION AND OUTLOOK

A reliable flight dynamics model for the Penguin BE aircraft used in cooperative landing tests has been developed, with some inaccuracies in vertical velocity, w . An analysis of the pitch attitude control design that is currently in use has been performed, which indicated similar performance of the control system applied to the actual system and its identified model. Furthermore, alternative control gains within the predefined specifications have been suggested.

In order to test the suitability of the identified model, additional validation experiments shall be defined and executed in the near future. If those are successful, new control laws shall be designed using the identified model. Once the techniques applied in this work have proven to yield adequate estimations, a lateral model shall also be identified. In addition, an engine model shall be obtained in order to reduce the mentioned inaccuracies, especially in throttle variation maneuvers. Ultimately, a global system identification procedure shall be carried out. This would account for the aircraft dynamics within the entire flight envelope. Once all the techniques needed to obtain a high-fidelity model of the Penguin BE UAV are mastered, the first attempts to model flexible HALE aircraft for stratospheric missions shall be performed.

Bibliography

ACKERMANN, J. Parameter space design of robust control systems. *IEEE Transactions on Automatic Control*, IEEE, v. 25, n. 6, p. 1058–1072, 1980. Cited in page 24.

ACKERMANN, J. My experiences in the control field [historical perspectives]. *IEEE Control Systems*, v. 28, n. 6, p. 115–120, Dec 2008. ISSN 1066-033X. Cited in page 25.

ACKERMANN, J. *Robust control: Systems with uncertain physical parameters*. Berlin, Germany: Springer Science & Business Media, 2012. Cited in page 25.

BALMER, G. R. *Modelling and Control of a Fixed-wing UAV for Landings on a Mobile Landing Platform*. Dissertation (Master Thesis) — German Aerospace Center (DLR), Robotics and Mechatronics Center and KTH Royal Institute of Technology, 2015. Cited in pages 9, 12, 13, 16, and 27.

COOK, M. V. *Flight dynamics principles: a linear systems approach to aircraft stability and control*. 3rd. ed. [S.l.]: Butterworth-Heinemann, 2012. Cited in pages 15, 30, and 57.

DEMIREL, B.; GUVENC, L. Parameter space design of repetitive controllers for satisfying a robust performance requirement. *IEEE Transactions on Automatic Control*, IEEE, v. 55, n. 8, p. 1893–1899, 2010. Cited in page 25.

DRELA, M.; YOUNGREN, H. *XFOIL*: Subsonic airfoil development system. 2000. Available at: <<http://web.mit.edu/drela/Public/web/xfoil/>>. Accessed on: 10 Jul. 2017. Cited in page 12.

DRELA, M.; YOUNGREN, H. *Athena Vortex Lattice (AVL)*. 2004. Available at: <<http://web.mit.edu/drela/Public/web/avl/>>. Accessed on: 10 Jul. 2017. Cited in page 12.

EVANS, R. et al. Aircraft flight data compatibility checking using maximum likelihood and extended kalman filter estimation. *IFAC Proceedings Volumes*, Elsevier, v. 18, n. 5, p. 487–492, 1985. Cited in page 20.

FISHER, R. A. Theory of statistical estimation. *Mathematical Proceedings of the Cambridge Philosophical Society*, Cambridge University Press, v. 22, n. 5, p. 700–725, 1925. Cited in page 18.

FISHER, R. A. *Statistical methods for research workers*. 5th. ed. Edinburgh, UK: Oliver and Boyd, 1934. Cited in page 14.

FOURIER, J. B. J. *The Analytical Theory of Heat*. Cambridge, UK: Cambridge University Press, 1878. Cited in page 14.

GRYMIN, D. J. *Two-step system identification and primitive-based motion planning for control of small unmanned aerial vehicles*. Thesis (PhD) — Virginia Polytechnic Institute and State University, 2013. Cited in page 20.

- GRYMIN, D. J.; FARHOOD, M. Two-step system identification and trajectory tracking control of a small fixed-wing uav. *Journal of Intelligent & Robotic Systems*, Springer, v. 83, n. 1, p. 105–131, 2016. Cited in page 20.
- GUPTA, N. K.; HALL JR., W. E. Input design for identification of aircraft stability and control derivatives. *NASA Contractor Report 2493*, 1975. Cited in page 14.
- HAMEL, P. G.; JATEGAONKAR, R. V. Evolution of flight vehicle system identification. *Journal of aircraft*, v. 33, n. 1, p. 9–28, 1996. Cited in page 14.
- HARKEGARD, O.; GLAD, T. Vector backstepping design for flight control. In: AIAA. *AIAA guidance, navigation and control conference and exhibit*. Hilton Head, USA, 2007. p. 6421–6431. Cited in page 46.
- JATEGAONKAR, R. *Flight vehicle system identification: a time-domain methodology*. 2nd. ed. Reston, VA, USA: American Institute of Aeronautics and Astronautics, 2015. Cited in pages 14, 15, 16, 17, 18, 19, 20, 21, 23, and 28.
- KALETKA, J. et al. Time and frequency-domain identification and verification of bo 105 dynamic models. *15th EUROPEAN ROTORCRAFT FORUM*, n. 66, 1989. Cited in page 15.
- KASTNER, N.; LOOYE, G. Generic tecs based autopilot for an electric high altitude solar powered aircraft. In: IEEE. *EuroGNC 2013, 2nd CEAS Specialist Conference on Guidance, Navigation and Control*. Delft, Netherlands, 2013. Cited in page 9.
- KLÖCKNER, A. Geometry based flight dynamics modelling of unmanned airplanes. In: AIAA. *AIAA Modeling and Simulation Technologies (MST) Conference*. Boston, MA, USA, 2013. Cited in page 12.
- LAIACKER, M. et al. Vision aided automatic landing system for fixed wing uav. In: IEEE. *2013 IEEE/RSJ International Conference on Intelligent Robots and Systems*. Tokyo, Japan, 2013. p. 2971–2976. Cited in page 9.
- LAVRETSKY, E.; WISE, K. A. Robust adaptive control. In: . London, UK: Springer, 2013. p. 317–353. Cited in page 25.
- LEE, J. *High Fidelity Modelling for High Altitude Long Endurance Solar Powered Aircraft*. Dissertation (Master Thesis) — German Aerospace Center (DLR), Robotics and Mechatronics Center and ETH Zurich, 2017. Cited in pages 5, 9, 10, 20, 23, 24, 28, 29, 41, 42, 44, and 46.
- LOMBAERTS, T. et al. Online aerodynamic model structure selection and parameter estimation for fault-tolerant control. *Journal of guidance, control, and dynamics*, v. 33, n. 3, p. 707, 2010. Cited in page 19.
- MARTIN, C.; FEIK, R. Estimation of aircraft dynamic states and instrument systematic errors from flight test measurements. In: CONFERENCE ON CONTROL ENGINEERING. *Second Conference on Control Engineering 1982: Merging of Technology and Theory to Solve Industrial Automation Problems; Preprints of Papers*. Newcastle, UK, 1982. p. 174. Cited in page 20.

MEHRA, R. Optimal input signals for parameter estimation in dynamic systems—survey and new results. *IEEE Transactions on Automatic Control*, IEEE, v. 19, n. 6, p. 753–768, 1974. Cited in page 14.

MILLER, H.; MATTUCK, A. *18.03 Differential Equations*: chapter 13. 2010. Available at: <https://ocw.mit.edu/courses/mathematics/18-03-differential-equations-spring-2010/readings/supp_notes/MIT18_03S10_chapter_13.pdf>. Accessed on: 26 Jun. 2017. Cited in page 30.

MILLIKEN JR., W. F. Progress in dynamic stability and control research. *Journal of the Aeronautical Sciences*, v. 14, n. 9, p. 493–519, 1947. Cited in page 14.

MORELLI, E. A.; KLEIN, V. et al. Application of system identification to aircraft at nasa langley research center. *Journal of Aircraft*, v. 42, n. 1, p. 12–25, 2005. Cited in page 16.

MULDER, J. et al. Non-linear aircraft flight path reconstruction review and new advances. *Progress in Aerospace Sciences*, Elsevier, v. 35, n. 7, p. 673–726, 1999. Cited in page 19.

MUSKARDIN, T. et al. A novel landing system to increase payload capacity and operational availability of high altitude long endurance uav. In: IEEE. *2016 IEEE International Conference on Unmanned Aircraft Systems (ICUAS)*. Arlington, USA, 2016. p. 495–504. Cited in page 9.

MUSKARDIN, T. et al. A novel landing system to increase payload capacity and operational availability of high altitude long endurance uavs. *Journal of Intelligent & Robotic Systems*, Jan 2017. Cited in pages 9 and 10.

MUSKARDIN, T. et al. Landing of a fixed-wing uav on a mobile ground vehicle. In: IEEE. *2016 IEEE International Conference on Robotics and Automation (ICRA)*. Stockholm, Sweden, 2016. p. 1237–1242. Cited in page 9.

OLIVEIRA, J. et al. Output error method and two step method for aerodynamic model identification. In: AIAA. *AIAA Guidance, Navigation, and Control Conference*. San Francisco, USA, 2005. Cited in page 20.

PERSSE, L. *Cooperative Control for Landing a Fixed-Wing Unmanned Aerial Vehicle on a Ground Vehicle*. Dissertation (Master Thesis) — German Aerospace Center (DLR), Robotics and Mechatronics Center and KTH Royal Institute of Technology, 2016. Cited in pages 9 and 12.

PLAETSCHKE, E.; SCHULZ, G. Practical input signal design. *AGARD Lecture Series*, v. 104, 1979. Cited in pages 14 and 16.

QIAN, J.; NADRI, M.; DUFOUR, P. Optimal input design for parameter estimation of nonlinear systems: case study of an unstable delta wing. *International Journal of Control*, v. 90, n. 4, p. 873–887, 2017. Cited in page 14.

SAEKI, M. Rendering of unfalsified pid gain sets for parameter space control design. In: IEEE. *9th Asian Control Conference (ASCC)*. Istanbul, Turkey, 2013. p. 1–6. Cited in page 25.

SCHLESINGER, S. et al. Developing standard procedures for simulation validation and verification (autopilot, atmosphere and transportation models). In: *Summer Computer Simulation Conference*. Houston, USA: [s.n.], 1974. p. 927–933. Cited in page 23.

SHANNON, C. E. A mathematical theory of communication. *Bell System Technical Journal*, v. 27, n. 4, p. 379–423, 623–656, 1948. Cited in page 14.

TEIXEIRA, B. O. et al. Flight path reconstruction—a comparison of nonlinear kalman filter and smoother algorithms. *Aerospace Science and Technology*, Elsevier, v. 15, n. 1, p. 60–71, 2011. Cited in page 19.

UAV FACTORY. *Penguin BE Electric Unmanned Platform*: Datasheet. Irvington, NY, USA. Cited in pages 10 and 11.

UNMANNED DYNAMICS. *AeroSim – aeronautical simulation blockset*: User’s guide. Hood River, OR, USA. Cited in page 12.

WANG, K. C.; ILIFF, K. Retrospective and recent examples of aircraft parameter identification at nasa dryden flight research center. *Journal of Aircraft*, American Institute of Aeronautics and Astronautics (AIAA), v. 41, n. 4, 2004. Cited in page 16.

Appendix

APPENDIX A – CONCISE LONGITUDINAL AERODYNAMIC DERIVATIVES AND ENGINE DYNAMICS

Table 22 shows the definition of the concise derivatives (COOK, 2012).

Table 22 – Definition of the concise derivatives.

Concise derivative	Definition
x_u	Concise axial force derivative with respect to velocity along the x-axis
x_w	Concise axial force derivative with respect to velocity along the z-axis
x_q	Concise axial force derivative with respect to pitch rate
x_θ	Concise axial force derivative with respect to pitch angle
x_ω	Concise axial force derivative with respect to motor angular velocity
x_{δ_e}	Concise axial force derivative with respect to elevator command
z_u	Concise normal force derivative with respect to velocity along the x-axis
z_w	Concise normal force derivative with respect to velocity along the z-axis
z_q	Concise normal force derivative with respect to pitch rate
z_θ	Concise normal force derivative with respect to pitch angle
z_{δ_e}	Concise normal force derivative with respect to elevator command
m_u	Concise pitching moment derivative with respect to velocity along the x-axis
m_w	Concise pitching moment derivative with respect to velocity along the z-axis
m_q	Concise pitching moment derivative with respect to pitch rate
m_ω	Concise pitching moment derivative with respect to motor angular velocity
m_{δ_e}	Concise pitching moment derivative with respect to elevator command

Source: The author.

Engine dynamics is assumed to follow Equation A.1.

$$\omega(s) = k_u \frac{u(s)}{s} + k_w \frac{w(s)}{s} + \frac{k_\omega}{1 + T_\omega s} \delta_t(s) \quad (\text{A.1})$$

where argument (s) indicates that variables are in frequency domain. k_u , k_w , and k_ω are gains, and T_ω is the time constant of the system whose input is δ_t and output is ω .

This equation has been obtained by performing the Laplace transform of the fifth line of the *a priori* model, presented in Section 2.1.